ACS NANO

www.acsnano.org

ARTICLE

Simultaneous Photonic and Excitonic Coupling in Spherical Quantum Dot Supercrystals

Emanuele Marino, Alice Sciortino, Annemarie Berkhout, Katherine E. MacArthur, Marc Heggen, Tom Gregorkiewicz, Thomas E. Kodger, Antonio Capretti, Christopher B. Murray, A. Femius Koenderink, Fabrizio Messina, and Peter Schall*

Cite This: *ACS Nano* 2020, 14, 13806–13815

Read Online

ACCESS | Metrics & More | Article Recommendations | Supporting Information

ABSTRACT: Semiconductor nanocrystals, or quantum dots (QDs), simultaneously benefit from inexpensive low-temperature solution processing and exciting photophysics, making them the ideal candidates for next-generation solar cells and photodetectors. While the working principles of these devices rely on light absorption, QDs intrinsically belong to the Rayleigh regime and display optical behavior limited to electric dipole resonances, resulting in low absorption efficiencies. Increasing the absorption efficiency of QDs, together with their electronic and excitonic coupling to enhance charge carrier mobility, is therefore of critical importance to enable practical applications. Here, we demonstrate a general and scalable approach to increase both light absorption and excitonic coupling of QDs by fabricating hierarchical metamaterials. We assemble QDs into crystalline supraparticles using an emulsion template and demonstrate that these colloidal supercrystals (SCs) exhibit extended resonant optical behavior resulting in an enhancement in absorption efficiency in the visible range of more than 2 orders of magnitude with respect to the case of dispersed QDs. This successful light trapping strategy is complemented by the enhanced excitonic coupling observed in ligand-exchanged SCs, experimentally demonstrated through ultrafast transient absorption spectroscopy and leading to the formation of a free biexciton system on sub-picosecond time scales. These results introduce a colloidal metamaterial designed by self-assembly from the bottom up, simultaneously featuring a combination of nanoscale and mesoscale properties leading to simultaneous photonic and excitonic coupling, therefore presenting the nanocrystal analogue of supramolecular structures.

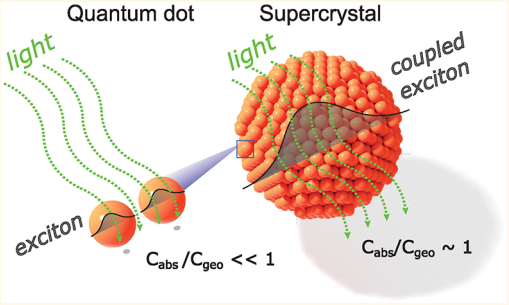

KEYWORDS: *self-assembly, supraparticles, supercrystals, nanocrystals, quantum dots, Mie theory, transient absorption*

Understanding and controlling the interaction of light with matter arguably represents one of the most intriguing and rewarding scientific challenges of direct importance to technological advances. Both solar energy harvesting techniques and telecommunications rely on the conversion of light into electricity and vice versa, for which interesting possibilities arise at the nanoscale, the size regime intermediate between molecular and bulk materials. In this respect, quantum dots (QDs), semiconductor crystals of a few nanometers in diameter, are the ideal building blocks for next-generation optoelectronic devices. The rich photophysics of QDs can raise the maximum power conversion efficiency of solar cells by harvesting high energy carriers,[1,2] while their size-tunable band gap enables the fabrication of high-sensitivity photodetectors active from the ultraviolet to the infrared.[3,4]

While all these advances are enabled at the nanoscale, the nanoscopic dimensions of QDs also represent a limitation to the performance of solar cells and photodetectors. The working principles of these devices intrinsically rely on the efficient generation of electron–hole pairs through light absorption. The efficiency of light absorption at a wavelength λ is often described by normalizing the absorption cross section of the absorbing material, $C_{abs}(\lambda)$, by its geometric cross section, C_{geo}. Therefore, if a uniform beam of light impinges on an isolated QD, only the photons impinging on the area fraction $C_{abs}(\lambda)/C_{geo}$ will result in absorption, as illustrated in Figure 1a (left). As subwavelength dielectric

Received: July 23, 2020
Accepted: September 14, 2020
Published: September 14, 2020

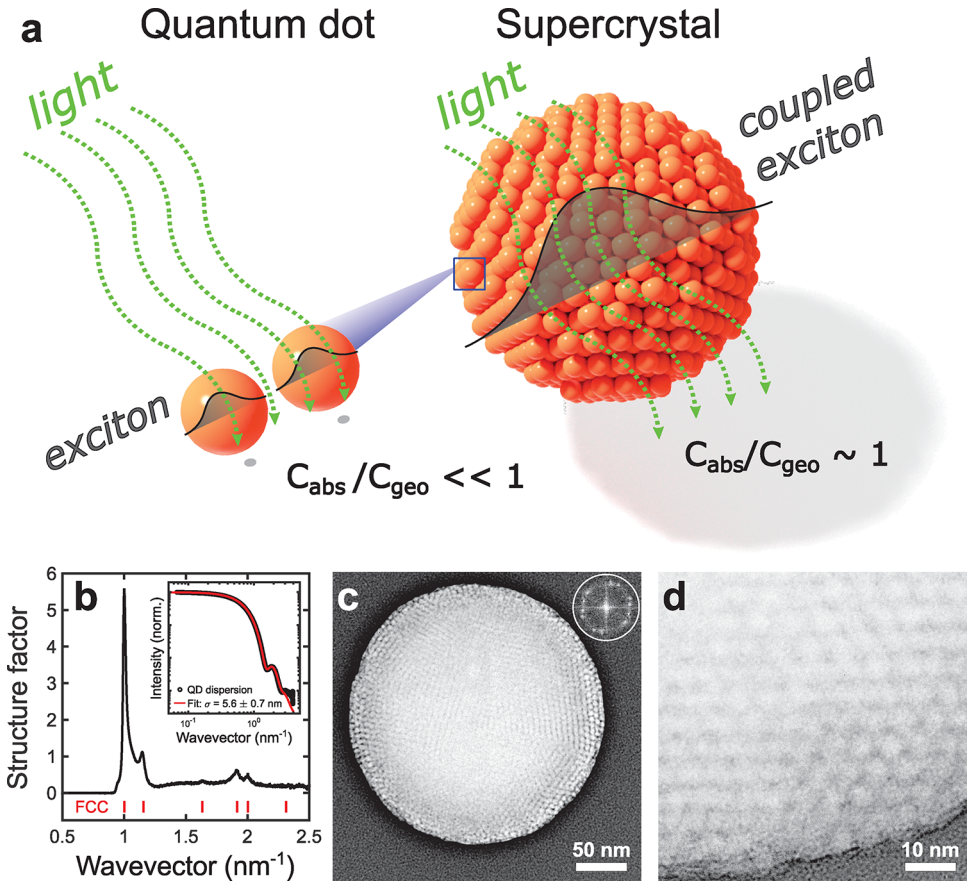

Figure 1. Quantum dot supercrystals (QD SCs) and their interaction with light. (a) Schematic representation of the interaction of light with dispersed QDs (left) and a QD SC (right). As dielectric nanoparticles, QDs feature low absorption efficiencies, $C_{abs}/C_{geo} \ll 1$, while assembling QDs into SCs results in resonant light-matter photonic coupling and more efficient light absorption, $C_{abs}/C_{geo} \sim 1$. Furthermore, the close-packed arrangement of QDs promotes interdot excitonic coupling. (b–d) Structure and morphology of the fabricated CdSe QD SCs. (b) Structure factor of QD SCs extracted from the small-angle X-ray scattering pattern of a dispersion of QD SCs. Inset: Form factor as measured from a dilute dispersion of the CdSe QDs. (c) Transmission electron micrograph of a single QD SC. The inset shows the fast-Fourier transform of the SC, revealing 6-fold symmetry. (d) Transmission electron micrograph showing QD ordering near the surface of the SC.

nanoparticles, QDs intrinsically feature low absorption cross sections: a CdSe QD of diameter σ = 5.5 nm features an absorption efficiency of $C_{abs}(\lambda)/C_{geo} \approx 0.01 \ll 1$ at λ = 400 nm.[5] Consequently, increasing the absorption efficiency of QDs to reach values of the order of $C_{abs}/C_{geo} \sim 1$ represents an issue of critical importance. However, from a device-oriented perspective, increasing the efficiency of light absorption only brings a partial advantage. In fact, a critical feature of QDs is that the excitons generated by the light absorption are tightly confined to the volume of the QD where they are generated, making the transport and extraction of free carriers from a device a modern challenge.[6−9] To facilitate this transport, there is a need to develop a unified strategy to concomitantly enhance the absorption efficiency and interdot coupling in QDs. Succeeding in this respect would enable QD-based applications, such as photodetectors with single-photon sensitivity,[10,11] and serve as a test bed for future developments in excitonics.[12]

Recently, emulsion-templated assembly has emerged as a scalable approach to fabricate supraparticles, mesoscale colloids composed of smaller building blocks.[13−16] Due to their ease of fabrication and sizes comparable to the wavelength of light, these supraparticles provide a viable colloidal alternative to expensive lithography-based structures such as resonators.[17,18]

In this work, we use this emulsion-based approach to fabricate a hierarchical metamaterial simultaneously featuring photonic and excitonic coupling, therefore demonstrating a general route to enhance the absorption efficiency and interdot coupling in QDs. We fabricate spherical supraparticles consisting of ordered QDs, and show that these supercrystals (SCs) focus intense electromagnetic fields to subwavelength regions, resulting in sharp optical resonances spectrally tunable by varying SC diameter. By combining optical spectroscopy and microscopy, and modeling of these resonances through Mie theory, we find that QD SCs reach absorption efficiencies greater than unity in the visible spectral range and for a wide distribution of SC diameters, effectively collecting light from an area larger than their geometric cross section, Figure 1a (right).[20] To concomitantly increase the excitonic coupling in these photonically active SCs, we decrease the interdot distance through ligand exchange; as a consequence, the biexciton transits from a bound to a free state. This demonstration of a metamaterial simultaneously featuring intrinsic photonic and excitonic coupling offers a perspective for devices based on bottom-up self-assembled QDs.

https://dx.doi.org/10.1021/acsnano.0c06188
ACS Nano 2020, 14, 13806−13815

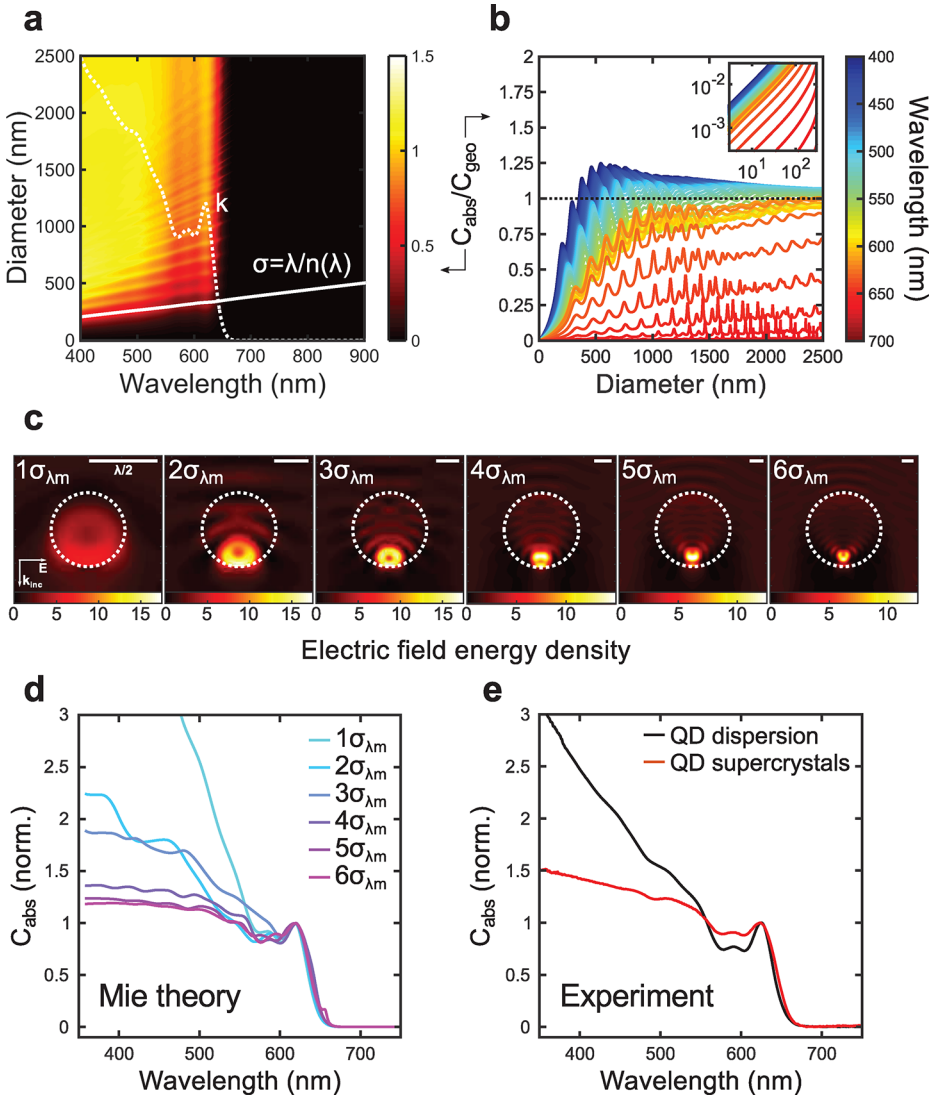

Figure 2. Absorption cross section of QD SCs in air based on Mie theory and experimentally measured. (a) Map of the absorption efficiency of CdSe QD SCs as a function of excitation wavelength, λ, and SC diameter, σ, as modeled from Mie theory. The dotted white line describes the imaginary part of the refractive index of QDs used in the modeling, k, while the full white line describes the resonant threshold $\sigma = \lambda/n(\lambda)$. (b) Size cuts of the absorption efficiency of QD SCs for various excitation wavelengths in the visible range. The inset shows that for $\sigma \ll \lambda/n$ the Rayleigh behavior is retained: $C_{abs}/C_{geo} \sim \sigma$.[30] (c) Map of the electric field energy density, $u_E \approx n(\lambda)^2|E|^2$, within and in proximity of QD SCs for λ = 400 nm. The geometric cross sections of SCs are outlined by the dotted white lines, with diameters $i\sigma_{\lambda_m} = i\lambda_m/n(\lambda_m) \approx i220$ nm, i = 1−6. The directions of the incident plane wave, k_{inc}, and of the electric field, E, are specified in the inset. Scale bars indicate $\lambda/2$. The absorption cross section density is obtained by multiplying u_E by $[n(\lambda)\,k(\lambda)]/[n(\lambda)^2 - k(\lambda)^2] \approx 0.05$ at λ = 400 nm. (d) Spectral cuts of the absorption cross section of QD SCs for diameters matching (c). (e) Experimentally determined absorption cross sections of QDs dispersed (black) and assembled into SCs (red). The cross section values in (d) and (e) have been normalized to the first exciton peak to enable comparison between modeled and experimental data.

RESULTS AND DISCUSSION

We synthesize spherical CdSe QDs with a diameter of σ_{QD} = 5.6 ± 0.7 nm as determined from their form factor measured with small-angle X-ray scattering (Figure 1b).[21] These QDs are then assembled into spherical supraparticles using an emulsion template;[13−16] due to the polydisperse nature of the emulsion droplets, the resulting supraparticles are also polydisperse, with a mean diameter of $\sigma \approx 240$ nm, Figure S1. While a multitude of techniques have been developed to assemble nanocrystals into two- and three-dimensional superstructures,[22−26] the emulsion template is particularly valuable as it allows the formation of structurally ordered supraparticles, or SCs, with grain sizes >600 nm by imposing exceptionally slow rates of solvent evaporation of the order of ∼1 μL/min,[27] therefore allowing the QDs to reach their minimum free energy configurations.[16,27−29] The diffraction pattern measured from a dispersion of these SCs features sharp reflections revealing a face-centered cubic (FCC) structure with an average crystalline grain size of $\xi \approx 276$ nm as extracted from the Scherrer equation, corresponding to $[\xi/(\sigma_{QD} + 2l)]^3\phi_{FCC} \approx 35000$ QDs per grain on average, where l = 1 nm is the thickness of the ligand shell[27] and ϕ_{FCC} = 0.74 is the volume fraction of a FCC crystal at close packing (Figure 1b). These results are further confirmed by transmission electron microscopy, showing spherical SCs with diameters comparable to the extracted grain size (Figure 1c,d),

https://dx.doi.org/10.1021/acsnano.0c06188
ACS Nano 2020, 14, 13806−13815

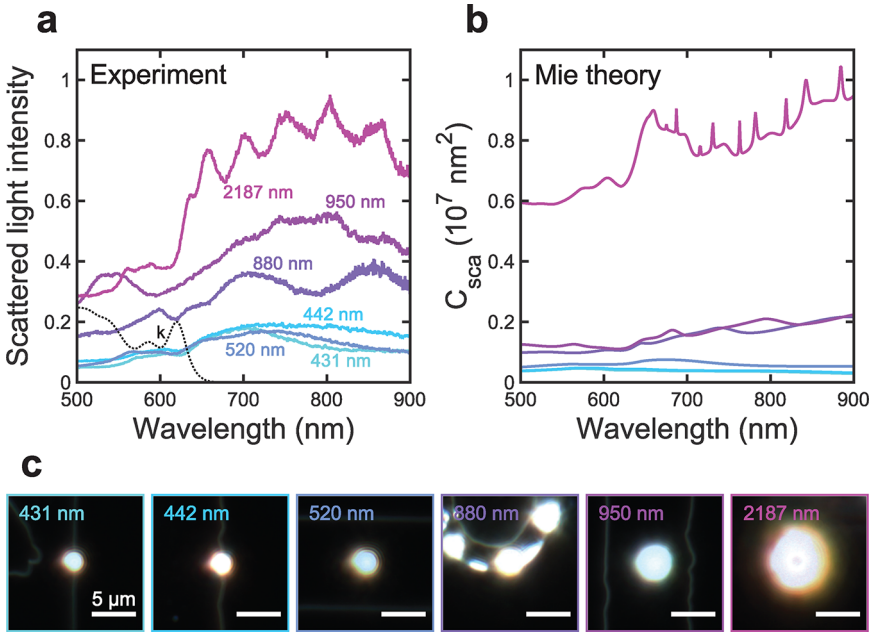

Figure 3. Experimental scattering spectra and simulated scattering cross sections of individual QD SCs. (a) Dark-field scattering spectra of individual QD SCs of various diameters determined by scanning electron microscopy (colored full lines, corresponding diameter indicated). The spectra were collected from SCs deposited on a lithographically checkerboard-patterned silicon substrate to allow accurate SC sizing in the electron microscope (Figure S6). For reference, the imaginary part of the refractive index of dispersed QDs, *k*, is shown (black dotted line). (b) Mie theory modeled scattering cross sections of individual QD SCs of diameters matching panel (a). To reproduce the embedding medium (air and silicon), we averaged the theoretical spectra of SCs embedded in air and in silicon (Figure S8).[47] (c) Dark-field images of the QD SCs investigated in panel (a). Light is collected from the solid angle subtended by a section 10 μm wide at the center of the image.

while for smaller diameters the structure appears disordered (Figure S11). The SC quality appears close to single-crystal, as suggested by the appearance of only two sets of spots with 6-fold symmetry in the fast-Fourier transform of the image.

Previous work has focused on using supraparticles as spherical resonators to manipulate light emission properties toward lasing applications.[19,31,32] Here instead, we investigate the potential of these spherical QD SCs as light-harvesting structures with light absorption properties intrinsically tailored through size. We provide a quantitative approach by using Mie theory that describes the interaction of light with a dielectric sphere.[30,33] The solution of Maxwell's equations for a plane wave of wavelength λ impinging on a dielectric sphere of diameter σ and complex refractive index $\tilde{n} = n + ik$ predicts the development of optical resonances, known as Mie modes, characterized by intense and localized electromagnetic fields when $\sigma \approx \lambda/n(\lambda)$.[34] Following Mie theory, we model the absorption efficiency by considering the QD SCs as spheres of a defined diameter obtained through scanning electron microscopy, and complex refractive index approximated by spectroscopic ellipsometry measurements on QD films, Figure 2a.[30,35,36] When exciting below the QD band gap, $\lambda > 620$ nm, the absorption efficiency drops to zero uniformly for all SC diameters as the imaginary part of the refractive index vanishes, indicated by the dotted white line. Above the band gap, $\lambda <$ 620 nm, the absorption efficiency increases quickly and is modulated by the wavelength dependence of the refractive index. This increase is marked by a distinct onset corresponding to the condition $\sigma = \lambda/n(\lambda)$, indicated by the full white line, clearly illustrating that the development of Mie modes, other than electric dipole, can only take place if the SC diameter is large enough to support the resonances: as the diameter increases, the absorption efficiency increases as well.

To investigate this behavior in detail, we show the absorption efficiency as a function of the SC diameter for a number of excitation wavelengths in Figure 2b. In the limit of SC diameters much smaller than the wavelength, $\sigma \ll \lambda/n(\lambda)$, we recover the Rayleigh limit and the absorption efficiency scales linearly with the SC diameter, $C_{abs}/C_{geo} \propto \sigma$, as shown in the inset.[30] Beyond this regime, given a fixed energy above the band gap, the absorption efficiency increases quickly with the SC diameter and reaches a maximum. Importantly, for a wide spectral region, $\lambda < 550$ nm, and a wide range of SC diameters, $\sigma > 350$ nm, the absorption efficiency reaches values well above unity, peaking at $C_{abs}/C_{geo} = 1.25$ for $\sigma_m = 550$ nm and $\lambda_m =$ 400 nm. Physically, this means that QD SCs can behave as "light funnels", absorbing light from an area up to 1.25 times their geometric cross section. When increasing the SC diameter further, the absorption efficiency decreases, plateauing at around $C_{abs}/C_{geo} = 1$. This is consistent with the reported behavior of Mie spheres in the limit of large diameters, often referred to as the *extinction and absorption paradox*.[30,37,38]

To elucidate the microscopic origin of this trend, we investigate the near-field behavior by calculating the spatial distribution of the electric field energy density, $u_E = \frac{\partial\epsilon(\omega)}{d\omega}|\mathbf{E}|^2 \approx n(\lambda)^2|\mathbf{E}|^2$, within and in proximity of QD SCs with diameters multiple of the optical size $\sigma_{\lambda_m} = \lambda_m/n(\lambda_m) \approx 220$ nm, Figure 2c.[30,35] In the smallest SC, $\sigma = \sigma_{\lambda_m}$, the electric field energy is distributed throughout the sphere, with most energy stored toward the back of the sphere. The linear dimensions of the storage volume are $\approx \lambda/2$, revealing that SCs can focus light to subwavelength regions. When increasing the SC diameter to $\sigma = 2\sigma_{\lambda_m}$, the dimensions of the storage volume do not vary significantly, while more energy per unit volume

https://dx.doi.org/10.1021/acsnano.0c06188
ACS Nano 2020, 14, 13806−13815

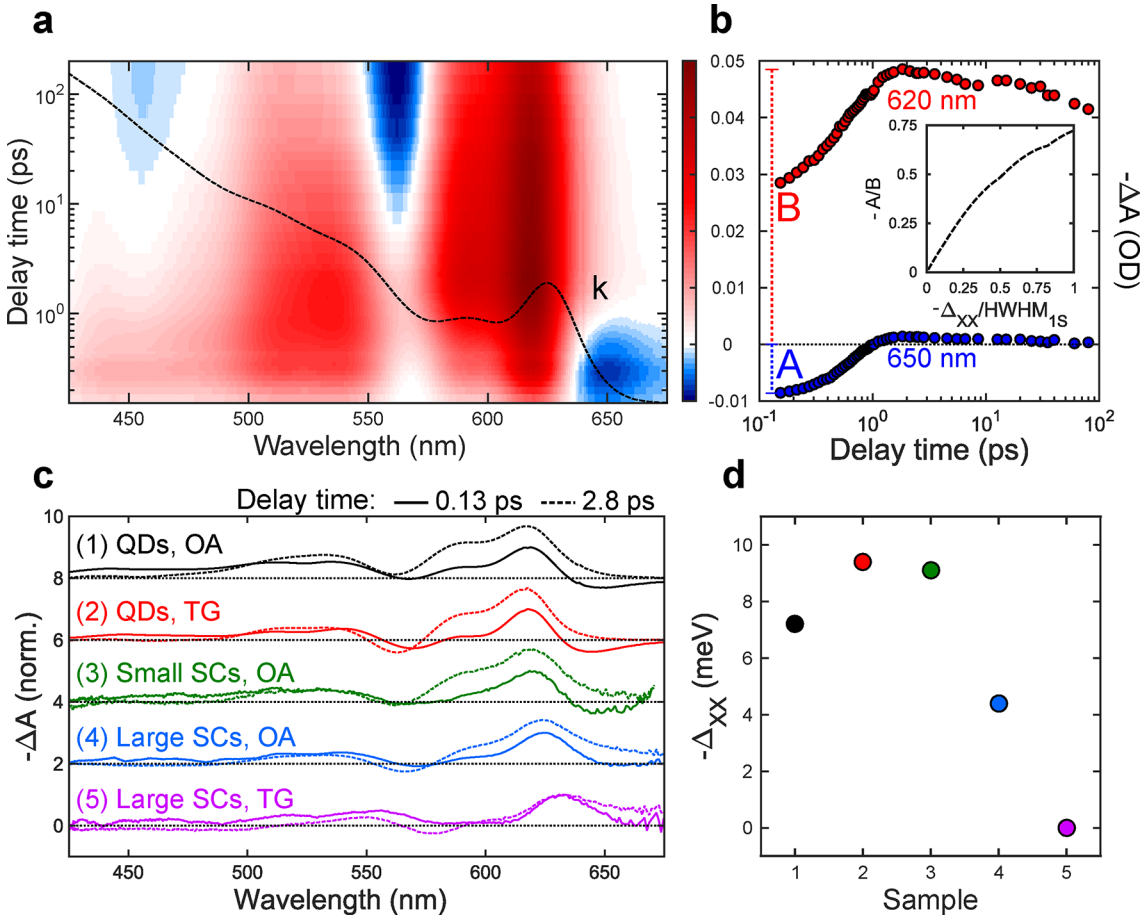

Figure 4. Ultrafast dynamics reveal enhanced excitonic coupling in QD SCs. (a) Map of the negative TA signal for oleate-capped QDs dispersed in hexane. The imaginary part of the refractive index, *k*, is also indicated (dotted line). (b) Temporal cuts of panel (a) showing the kinetic behavior at λ = 620 nm and 650 nm. The inset shows the expected dependence of the amplitude ratio *A*/*B* on the biexciton binding energy, Δ_{XX}, normalized to the half-width at half-maximum (HWHM) of the 1*S* transition.[50,52] (c) Spectral cuts of the negative TA signal at delay times 0.13 ps (full lines) and 2.8 ps (dashed lines) for different QD samples described in the text. (d) Values of biexciton binding energy, Δ_{XX}, extracted from the data shown in (c) and the expected values shown in the inset in (b).

can be stored at the back of the larger sphere, as indicated by the color map in Figure 2c. Eventually, the amount of energy per unit volume that can be stored in a SC peaks at $\sigma = 2.5\sigma_{\lambda_m} = \sigma_m$, and decreases for larger diameters. Distributions of the electric field density at the peak are shown in Figure S2. The maximum absorption efficiency is therefore limited by the penetration of the electric field within the SC and may be further optimized by tuning the refractive index by varying QD core material,[36,39] surface ligands,[40] architectural morphology,[8,41] and postprocessing treatments.[42]

While Figure 2c provides a visual illustration of the absorption efficiency and its saturation in the spectral range of λ < 550 nm, a quantitative prediction of the wavelength-dependent absorption cross section and its saturation for increasing SC diameters is shown in Figure 2d. These predictions are indeed in qualitative agreement with the experimental absorption cross section, shown in Figure 2e, measured from a polydisperse dispersion of SCs in solution, displaying a saturation of the absorbance for λ < 550 nm. Further confirmation comes from measurements of size-selected SCs, for which we obtain absorption curves very similar to the predicted ones, as shown in Figures S3 and S4. The experimentally measured absorption spectra of size-separated QD SCs show an increasing degree of saturation with increasing diameter, in good agreement with theory.

We further elucidate the photonic properties of QD SCs at the single SC level. While experimentally targeting the absorption efficiency of individual nanostructures in the size range 1−100 nm is very challenging,[43,44] estimating the scattering efficiency of larger superstructures is a more manageable task. By using a dark-field setup, we selectively collect the light scattered by individual QD SCs casted on a substrate, as shown in Figure S5.[45,46] We use a lithographically patterned silicon substrate to correlate the scattering spectrum of an individual SC, determined through dark-field spectroscopy, with its size, determined by scanning electron microscopy, as shown in Figure S6. As the SC diameter increases, the experimentally measured scattering spectra increase in intensity while developing an increasing number of peaks, as shown in Figure 3a (full lines). In the corresponding dark-field images, the SCs appear larger and brighter as a function of increasing diameter, Figure 3c. Interestingly, the intensity of all scattering spectra shows a strong increase for λ > 620 nm, with a local minimum corresponding to the first exciton peak of the CdSe QDs composing the SCs (dotted line). These observations can be rationalized: Larger SCs can support a larger number of

https://dx.doi.org/10.1021/acsnano.0c06188
ACS Nano 2020, 14, 13806−13815

multipole modes of the scattered field, therefore explaining the overall intensity increase with diameter. While the light exciting above the band gap interacts with the SCs through both absorption and scattering, below the band gap mainly scattering modes are excited. Therefore, the local maximum in absorption relative to the first exciton peak corresponds to a local minimum in scattering. As shown in Figures 3b and S7, the theoretical spectrally resolved scattering cross sections, C_{sca}, reproduce well the main features of the experimental spectra: The increase in intensity and number of peaks with diameter and the intensity increase below the band gap and even the local minimum at λ = 620 nm. We ascribe the dampening of the sharpest resonances to the presence of the silicon substrate, as elucidated in Figure S8 and in the Mie theory section in the Supporting Information. These SCs are thus metamaterials simultaneously displaying an interesting combination of nanoscale and mesoscale photonic behaviors: The complex refractive index is set by the choice of the constituent QDs and is ultimately determined by quantum confinement effects occurring at the nanoscale. Yet, the interaction of a SC with light is that of a dielectric sphere, resulting in enhanced absorption and scattering through Mie resonances typical of the mesoscale.

The enhancement in absorption efficiency of QD supraparticles resulting from their photonic nature may be instrumental to the design of optoelectronic devices based on photosensitivity, like photodetectors and solar cells, as well as to devices based on exciton manipulation.[12,48,49] However, for these devices to function, the initially generated charge carriers must be transported across the supraparticle, enabled by sufficiently strong coupling between neighboring QDs. We investigate this coupling by probing the kinetic occupation of electronic states by photogenerated charge carriers through transient absorption (TA) spectroscopy; TA uses a broad-band probe pulse to investigate the occupation of electronic states after high-energy excitation by a pump pulse (see schematic in Figure S9). A map of the TA signal showing the states occupied (red) and available (blue) to the probe pulse as a function of delay time for dispersed CdSe QDs is shown in Figure 4a. The rise of the bleach signal at λ = 620 nm describes the occupation of the first excited state of the electron, 1*S*, by intraband relaxation of high energy charge carriers initially excited by the λ = 400 nm pump pulse:[50,51] The time dependence shown in Figure 4b illustrates that this state filling takes place in about 2 ps, consistent with previous reports.[5] At the same time, a distinct photoinduced absorption (PA) signal develops at λ = 650 nm and vanishes within 1 ps. This PA feature indicates an electronic state arising from the binding of the pump-generated exciton with the probe-generated exciton into a biexciton.[50,51] The red shift of this state compared to the 1*S* transition is indicative of an attractive biexciton system characterized by a binding energy Δ_{XX} that can be experimentally estimated from the amplitude ratio between PA and bleach features, A/B, as illustrated in Figure 4b.[50] Monitoring the magnitude of Δ_{XX} therefore provides an opportunity to directly probe the excitonic coupling between QDs. In Figure 4c, we show the normalized spectral cuts measured at delay times 0.13 and 2.8 ps for QDs dispersed and assembled into SCs, while the two-dimensional TA maps are shown in Figure S10. From this, we calculate the values of Δ_{XX} indicated in Figure 4d. The biexciton binding energy for oleate (OA) capped QDs dispersed in hexane amounts to $\Delta_{XX} \sim -7.2$ meV, in agreement with previous TA experiments.[50,52] Replacing the long OA ligands with shorter thioglycolate (TG) ligands for dispersed QDs does not result in a decrease in $|\Delta_{XX}|$, as seen in Figure 4d samples 1 and 2. As expected, for isolated QDs the biexciton binding energy does not depend on the choice of surface ligand.

By contrast, the crystallization of QDs into SCs critically affects the binding energy, suggesting a mechanism of excitonic coupling between neighboring QDs. To clearly demonstrate this effect, we first isolate the fraction containing the smallest supraparticles from the polydisperse ensemble by centrifuging the dispersion at 3000*g* for 12 h and collecting the supernatant, resulting in a mean diameter of $\sigma \sim 130$ nm, Figure S11. These supraparticles do not display clear crystalline order, and can be rather described as amorphous. In this amorphous state of the QDs, the binding energy of biexcitons remains almost unchanged with respect to the dispersed QDs. However, for the ensemble of larger SCs with diameters up to $\sigma \sim 2.5$ μm, the binding energy decreases to $\Delta_{XX} \sim -4.4$ meV. Furthermore, after decreasing the interparticle distance between neighboring QDs through an exchange from native oleate to significantly shorter thioglycolate (TG) ligands, the PA feature vanishes, resulting in a nominally null binding energy.

We note that these changes cannot result from electrostatic screening effects due to the higher dielectric constant of the matrix surrounding a QD: hexane and *N*-methylformamide, solvents for, respectively, OA- and TG-capped QDs, have a ratio in a dielectric constant of ≈90 while still yielding similar values of Δ_{XX}. We also note that the decrease in $|\Delta_{XX}|$ cannot result from enhanced intraband cooling rates, since all samples show similar cooling time constants of 0.6−0.7 ps, as shown in Figure S12. Instead, we propose that the observed decrease in binding energy results from the increase in interdot excitonic coupling from isolated QDs to QD SCs. Specifically, the disappearance of the biexciton state suggests that the high-energy exciton excited by the pump delocalizes onto the neighboring QDs prior to the arrival of the probe pulse, that is, within 0.13 ps, the delay time of the earliest TA spectrum. This type of excitonic coupling is therefore intrinsically distinct from more conventional Förster resonant energy transfer or carrier trapping mechanisms.[53] In the dispersed state, the coupling of QDs is negligible as their average interdot distance is very large. This coupling is still negligible in the smallest supraparticles, likely because of their structural disorder. Instead, larger FCC SCs of OA-capped QDs feature 12 nearest neighbors with an average surface-to-surface distance of ≈2 nm,[27] increasing the probability of coupling events. The decrease in interdot distance due to the exchange to shorter TG ligands further enhances this coupling probability, resulting in a free biexciton system. This can be regarded as the fingerprint of the onset of excitonic coupling among neighboring QDs within the SC.

CONCLUSIONS

We have demonstrated the potential of QD SCs as supraparticles simultaneously featuring photonic and excitonic coupling. By directly measuring the absorption and scattering properties of SCs both in ensemble and at the single-particle level, and comparing to Mie theory, we have estimated that CdSe QD SCs can reach absorption efficiencies up to 1.25 in a wide spectral range in the visible and for a variety of sizes produced by emulsion-templated assembly, an increase of more than 2 orders of magnitude with respect to isolated QDs.

https://dx.doi.org/10.1021/acsnano.0c06188
ACS Nano 2020, 14, 13806−13815

This achievement is promising for the development of NC-based photonic structures that could result in efficient light-trapping strategies for solar cells and photodetectors not relying on any form of lithography. Furthermore, these supraparticles show enhanced excitonic coupling as we have shown directly by probing the path in energy-time space of photogenerated excitons. The decrease in the biexciton binding energy suggests a collective behavior of the SCs, in which exciton delocalization is favored by the degree of order in supraparticles and smaller interdot distances. Taken together, these results point to an optimized SC diameter of 550 nm simultaneously maximizing absorption efficiency and excitonic coupling upon excitation at 400 nm. These findings introduce the class of bottom-up Mie-tronics,[54] that will allow for the efficient production of photonically active structures with optical properties tailored by the choices of the constituent NC building blocks and resulting supraparticles.

METHODS

QD Synthesis. CdSe QDs were synthesized according to the literature with minor modifications.[21] Briefly, 3 mL of a 1 M TOP:Se solution was mixed with 7 mL of 1-octadecene (ODE) and loaded into a glass syringe placed in a syringe pump. Meanwhile, the cadmium oleate precursor solution was prepared by mixing 0.512 g of cadmium oxide, 6.28 g of oleic acid, and 25 g of ODE in a 100 mL round-bottom flask. While stirring, the reagents were degassed at 100 °C for 1 h. Afterward, the flask atmosphere was switched to nitrogen and the temperature raised to 260 °C. The temperature was held constant until the color of the mixture changed from dark-red to colorless. Subsequently, the temperature was dropped to 100 °C and the flask was placed under vacuum for 30 min. After switching the atmosphere again to nitrogen, the temperature was raised to 260 °C. Meanwhile, 0.063 g of Se powder was added to 5 mL of ODE and sonicated for 20 min. The Se/ODE mixture was injected at 260 °C by using a 22 mL plastic syringe equipped with a 16 G needle. Immediately thereafter, the temperature controller was set to 240 °C. 60 s after injection, the TOP:Se/ODE solution was added dropwise at a rate of 10 mL/h. At 60 min after injection, the reaction was quenched by removing the heating mantle and dropping the flask in a container full of room-temperature water while stirring. The reaction was split into enough 50 mL centrifuge tubes such that there were 5 mL of mixture in each tube. Approximately 20 mL of hexane was added to each tube which was then capped and vortexed. A volume of 25 mL of 200 proof ethanol was added to each tube, and the tubes were centrifuged at 8000*g* for 5 min. The QDs were washed twice more by redispersing the precipitate in 10 mL of hexane and then precipitating with an equal volume of ethanol. After the final wash, the QDs were redispersed in cyclohexane at a concentration of 50 mg/mL and filtered by using a 200 nm PTFE or PVDF syringe filter. A more detailed description of the synthesis is provided in the Supporting Information.

QD SC Synthesis and Ligand Exchange. QD SCs were synthesized by following our recently reported procedures for emulsion templating.[27,29] Briefly, we added 8 mL of 6 mg/mL sodium dodecyl sulfate in water to a 20 mL scintillation vial. Subsequently, we added 2 mL of a 5 mg/mL QD dispersion in cyclohexane. After capping the vial, we vortexed its contents for 30 s. The vial was then uncapped and, after the addition of a 1 in. stir bar, placed on a hot plate switched off and at room temperature. The emulsion was left to dry in the fume hood while stirring at 400 rpm. After drying for 12 h (overnight), we washed the resulting SCs twice by centrifuging at 3000*g* for 1 h, followed by redispersion in 6 mg/mL sodium dodecyl sulfate in water to reach a SC concentration of 5 mg/mL.

To ligand-exchange the QD SCs, we added 1 mL of QD SC stock dispersion to 9 mL of 10 mM sodium thioglycolate in water. The dispersion was left to stir at room temperature for 20 min, followed by rinsing twice with hexane. The rinsed dispersion was then centrifuged at 3000*g* for 20 min, and the pellet was redispersed in 1 mL of water. This washing step was repeated a second time, after which the pellet was redispersed in water.

Mie Theory Modeling. Mie theory calculations on dielectric spheres were done using *MatScat*, an open source software available at https://nl.mathworks.com/matlabcentral/fileexchange/36831-matscat.[35] The Mie calculations of energy density and field were independently verified using finite element modeling (COMSOL Multiphysics 5.2). We also tested the behavior of Mie resonances for spheroids of different aspect ratios by using SMARTIES, another open source software available at https://www.victoria.ac.nz/scps/research/research-groups/raman-lab/numerical-tools.[55] The complex refractive index for CdSe QDs was derived from ellipsometry data available in the literature for 5.1 nm CdSe QDs capped with oleic acid,[36] blue shifting the spectra by 8 nm to match the position of the first exciton peak in our samples. Specifically, the complex refractive index, $\tilde{n} = n + ik$, is reported in the supplementary spreadsheet of the publication of Diroll et al., page 1, columns A (wavelength, λ), T (real part of the refractive index, n), and U (imaginary part of the refractive index, k).[36] The value of the refractive index used for the near-field simulations was $\tilde{n}(\lambda = 400\ \text{nm}) = n + ik = 1.8173 + i0.0916$. The complex refractive index for silicon was also determined from the literature.[56]

Ensemble Optical Measurements. Optical absorption spectra were measured using a PerkinElmer Lambda 950 UV/vis/NIR spectrophotometer with integrating sphere. A 5 mg/mL dispersion of SC in 6 mg/mL sodium dodecyl sulfate in water was drop-casted on a quartz substrate followed by drying in air. The measurement was performed by placing the substrate at the center of the integrating sphere with an angle of 45° with respect to the incoming beam, so to allow for the collection of reflected, transmitted, and scattered light to quantify absorption.

Photolithography. The mask was custom-made by Delta Mask b.v., Enschede (The Netherlands). The mask is made of quartz, with a chromium coating. 12 × 12 mm^2 single-side polished silicon substrates were cleaned in acetone and sonicated in water, followed by cleaning with base piranha (15 min at 75 °C) and a final 60 s O_2 plasma descum step (Oxford Instruments Plasma Technologies Plasmalab 80 Plus). Next, the sample was spin-coated with HMDS as the adhesive layer, followed by spinning Ma-N1410 as optical resist. The target thickness was 1.5 μm. Next we exposed the sample using a Suss Mask aligner MA BA 6(365 nm i-line) at a nominal dose of 325 mJ/cm^2. After development, the sample was evaporated with 15 nm of Cr using PVD (Polyteknik Flextura M508E) and lift-off was done in 1-methyl-2-pyrrolidone at 60°C.

Dark-Field Microspectroscopy. Reflective dark field microscopy was performed using a home-built setup based on a Nikon universal illuminator unit (Nikon LV-UEPI 2 system) and a 100 W halogen lamp, equipped with objectives from the CFI LU Plan Fluor BD series (20× NA 0.45, 50× NA 0.8, and 100× NA 0.9). Samples were imaged with a f = 200 mm achromatic tube lens. Directly after the tube lens, a 70/30 beam splitter (Thorlabs BS022) directed 70% of the light onto the entrance facet of a collection fiber, while the remaining 30% was used to form an image on a CMOS color camera (Imaging Source DFK 21AU04). The collection fiber (Thorlabs M16L01, 50 μm core, NA 0.22) was multimode and led to an Avaspec 2048TEC-2-USB2 spectrometer (thermoelectrically cooled 2048 pixel Si CCD, 600 l/mm grating, 75 mm focal length) with a resolving power of around 0.3 nm/pixel and a detection range from 500 to 1000 nm. No polarization optics were used. The spectra in this work were collected with the 100× objective, with illumination through the objective reflective mantle at angles just beyond the collection NA. Sample preparation consisted in 2 min of plasma cleaning of the lithographically patterned substrates, followed by spin-coating (1500 rpm, 30 s and 3000 rpm, 10 s) of a dispersion of CdSe QD SCs (5×10^{-3} g/L) in water (sodium dodecyl sulfate 6 g/L). Further details are provided in the Supporting Information.

Ultrafast Transient Absorption Spectroscopy. Femtosecond transient absorption (TA) measurements were based on a 5 kHz Ti:sapphire femtosecond amplifier (Spectra Physics Solstice-Ace)

https://dx.doi.org/10.1021/acsnano.0c06188
ACS Nano 2020, 14, 13806−13815

which produces 75 fs pulses peaking at λ = 800 nm (fwhm = 30 nm) at 350 μJ/pulse. This beam was split in two parts by using a beam splitter (80%/20%) to generate the pump and the probe, respectively. The pump (λ = 400 nm) was produced by frequency-doubling the fundamental λ = 800 nm (type I phase-matching) in a 250 μm β-BBO crystal. The pump beam was chopped at 500 Hz and focused on a 200 μm light path quartz flow cell by a parabolic mirror with f = 150 mm. Its polarization was controlled with a waveplate. A probe beam consisted of a supercontinuum pulse (λ = 400−700 nm) generated by focusing the λ = 800 nm beam on a D_2O-filled 1 mm light path quartz cuvette. The probe was focused on the sample by the same parabolic mirror used to focus the pump. The pump−probe delay was controlled with a motorized delay stage which yields a temporal resolution of 70 fs. The probe and the pump overlapped within the same volume of the sample. The sample was flowed through a 200 μm light path quartz flow cell at a rate of 20 mL/h. The sample concentration was kept at 1 mg/mL for all measurements to minimize scattering. After the sample flow cell, the probe beam was dispersed by a Brewster angle silica prism and focused on the detector by a lens. The spectral resolution is 3 nm. The pump and probe were synchronized with a camera detector system with 1024 pixels (Glaz Linescan-I) with single-shot capability. A typical signal was obtained by averaging 5000 pumped and 5000 unpumped spectra for each delay and scanning over the pump−probe delay 40 times.

ASSOCIATED CONTENT

Supporting Information

The Supporting Information is available free of charge at https://pubs.acs.org/doi/10.1021/acsnano.0c06188.

Detailed description of procedures for QD synthesis, small-angle X-ray scattering, electron microscopy, Mie theory modeling, photolithography, optical measurements; STEM images of QD supercrystals; size fractionation of QD supercrystals; absorption spectra of each fraction; schematic of dark-field setup; theoretical scattering efficiency map of QD supercrystals; exciton cooling kinetics as measured by TA (PDF)

AUTHOR INFORMATION

Corresponding Author

Peter Schall − *Van der Waals−Zeeman Institute, University of Amsterdam, 1098XH Amsterdam, The Netherlands;* Email: p.schall@uva.nl

Authors

Emanuele Marino − *Van der Waals−Zeeman Institute, University of Amsterdam, 1098XH Amsterdam, The Netherlands; Department of Chemistry, University of Pennsylvania, Philadelphia, Pennsylvania 19104, United States;* orcid.org/0000-0002-0793-9796

Alice Sciortino − *Dipartimento di Fisica e Chimica−Emilio Segrè, Università degli Studi di Palermo, 90123 Palermo, Italy;* orcid.org/0000-0001-8361-3002

Annemarie Berkhout − *Center for Nanophotonics, AMOLF, 1098XG Amsterdam, The Netherlands*

Katherine E. MacArthur − *Ernst Ruska Centre for Microscopy and Spectroscopy with Electrons and Peter Grünberg Institute, Forschungszentrum Jülich GmbH, 52425 Jülich, Germany;* orcid.org/0000-0002-5024-2054

Marc Heggen − *Ernst Ruska Centre for Microscopy and Spectroscopy with Electrons and Peter Grünberg Institute, Forschungszentrum Jülich GmbH, 52425 Jülich, Germany*

Tom Gregorkiewicz − *Van der Waals−Zeeman Institute, University of Amsterdam, 1098XH Amsterdam, The Netherlands;* orcid.org/0000-0003-2092-8378

Thomas E. Kodger − *Physical Chemistry and Soft Matter, Wageningen University and Research, 6708WE Wageningen, The Netherlands; Van der Waals−Zeeman Institute, University of Amsterdam, 1098XH Amsterdam, The Netherlands*

Antonio Capretti − *Van der Waals−Zeeman Institute, University of Amsterdam, 1098XH Amsterdam, The Netherlands*

Christopher B. Murray − *Department of Chemistry and Department of Materials Science and Engineering, University of Pennsylvania, Philadelphia, Pennsylvania 19104, United States*

A. Femius Koenderink − *Center for Nanophotonics, AMOLF, 1098XG Amsterdam, The Netherlands; Van der Waals−Zeeman Institute, University of Amsterdam, 1098XH Amsterdam, The Netherlands;* orcid.org/0000-0003-1617-5748

Fabrizio Messina − *Dipartimento di Fisica e Chimica−Emilio Segrè, Università degli Studi di Palermo, 90123 Palermo, Italy;* orcid.org/0000-0002-2130-0120

Complete contact information is available at: https://pubs.acs.org/10.1021/acsnano.0c06188

Notes

The authors declare no competing financial interest.

ACKNOWLEDGMENTS

This work is part of the research programme "Nano-architectures: Smart Assembly, Quantum Electronics and Soft Mechanics" with Project Number 680.47.615, which is financed by the Dutch Research Council (NWO). E.M. and C.B.M. acknowledge financial support from the Office of Naval Research Multidisciplinary University Research Initiative Award ONR N00014-18-1-2497. P.S., T.E.K., and A.F.K. acknowledge financial support from NWO through personal Vici, Veni, and Vici grants, respectively. Beamtime at BM26B "DUBBEL" beamline, ESRF, was supported through NWO funding, experiment number 26-02-841. The authors thank Bob Drent for the fabrication of the lithographic template and Gianluca Grimaldi for useful discussions.

REFERENCES

(1) Ross, R. T.; Nozik, A. J. Efficiency of Hot-Carrier Solar Energy Converters. *J. Appl. Phys.* **1982**, *53*, 3813−3818.

(2) Grimaldi, G.; Crisp, R. W.; ten Brinck, S.; Zapata, F.; van Ouwendorp, M.; Renaud, N.; Kirkwood, N.; Evers, W. H.; Kinge, S.; Infante, I.; et al. Hot-Electron Transfer in Quantum-Dot Heterojunction Films. *Nat. Commun.* **2018**, *9*, 2310−2319.

(3) Saran, R.; Curry, R. J. Lead Sulphide Nanocrystal Photodetector Technologies. *Nat. Photonics* **2016**, *10*, 81−92.

(4) Tang, X.; Ackerman, M. M.; Chen, M.; Guyot-Sionnest, P. Dual-Band Infrared Imaging Using Stacked Colloidal Quantum Dot Photodiodes. *Nat. Photonics* **2019**, *13*, 277−282.

(5) Klimov, V. I. Optical Nonlinearities and Ultrafast Carrier Dynamics in Semiconductor Nanocrystals. *J. Phys. Chem. B* **2000**, *104*, 6112−6123.

(6) Ganesan, A. A.; Houtepen, A. J.; Crisp, R. W. Quantum Dot Solar Cells: Small Beginnings Have Large Impacts. *Appl. Sci.* **2018**, *8*, 1867−1894.

(7) Lee, E. M. Y.; Tisdale, W. A.; Willard, A. P. Perspective: Nonequilibrium Dynamics of Localized and Delocalized Excitons in Colloidal Quantum Dot Solids. *J. Vac. Sci. Technol., A* **2018**, *36*, 068501.

(8) Marino, E.; Balazs, D. M.; Crisp, R. W.; Hermida-Merino, D.; Loi, M. A.; Kodger, T. E.; Schall, P. Controlling Superstructure-Property Relationships *via* Critical Casimir Assembly of Quantum Dots. *J. Phys. Chem. C* **2019**, *123*, 13451−13457.
(9) Ginsberg, N. S.; Tisdale, W. A. Spatially Resolved Exciton and Charge Transport in Emerging Semiconductors. *Annu. Rev. Phys. Chem.* **2020**, *71*, 1−30.
(10) Anikeeva, P. O.; Halpert, J. E.; Bawendi, M. G.; Bulović, V. Electroluminescence from a Mixed Red-Green-Blue Colloidal Quantum Dot Monolayer. *Nano Lett.* **2007**, *7*, 2196−2200.
(11) Komiyama, S.; Astafiev, O.; Antonov, V.; Kutsuwa, T.; Hirai, H. A Single-Photon Detector in the Far-Infrared Range. *Nature* **2000**, *403*, 405−407.
(12) Unuchek, D.; Ciarrocchi, A.; Avsar, A.; Watanabe, K.; Taniguchi, T.; Kis, A. Room-Temperature Electrical Control of Exciton Flux in a van der Waals Heterostructure. *Nature* **2018**, *560*, 340−344.
(13) Velev, O. D.; Lenhoff, A. M.; Kaler, E. W. A Class of Microstructured Particles through Colloidal Crystallization. *Science* **2000**, *287*, 2240−2243.
(14) Manoharan, V. N.; Elsesser, M. T.; Pine, D. J. Dense Packing and Symmetry in Small Clusters of Microspheres. *Science* **2003**, *301*, 483−487.
(15) Lacava, J.; Born, P.; Kraus, T. Nanoparticle Clusters with Lennard-Jones Geometries. *Nano Lett.* **2012**, *12*, 3279−3282.
(16) de Nijs, B.; Dussi, S.; Smallenburg, F.; Meeldijk, J. D.; Groenendijk, D. J.; Filion, L.; Imhof, A.; van Blaaderen, A.; Dijkstra, M. Entropy-Driven Formation of Large Icosahedral Colloidal Clusters by Spherical Confinement. *Nat. Mater.* **2015**, *14*, 56−60.
(17) Le-Van, Q.; Le Roux, X.; Aassime, A.; Degiron, A. Electrically Driven Optical Metamaterials. *Nat. Commun.* **2016**, *7*, 12017−12023.
(18) le Feber, B.; Prins, F.; De Leo, E.; Rabouw, F. T.; Norris, D. J. Colloidal-Quantum-Dot Ring Lasers with Active Color Control. *Nano Lett.* **2018**, *18*, 1028−1034.
(19) Montanarella, F.; Urbonas, D.; Chadwick, L.; Moerman, P. G.; Baesjou, P. J.; Mahrt, R. F.; van Blaaderen, A.; Stöferle, T.; Vanmaekelbergh, D. Lasing Supraparticles Self-Assembled from Nanocrystals. *ACS Nano* **2018**, *12*, 12788−12794.
(20) Brongersma, M. L.; Cui, Y.; Fan, S. Light Management for Photovoltaics Using High-Index Nanostructures. *Nat. Mater.* **2014**, *13*, 451−460.
(21) Chernomordik, B. D.; Marshall, A. R.; Pach, G. F.; Luther, J. M.; Beard, M. C. Quantum Dot Solar Cell Fabrication Protocols. *Chem. Mater.* **2017**, *29*, 189−198.
(22) Shevchenko, E. V.; Talapin, D. V.; Kotov, N. A.; O'Brien, S.; Murray, C. B. Structural Diversity in Binary Nanoparticle Superlattices. *Nature* **2006**, *439*, 55−59.
(23) Mueggenburg, K. E.; Lin, X.-M.; Goldsmith, R. H.; Jaeger, H. M. Elastic Membranes of Close-Packed Nanoparticle Arrays. *Nat. Mater.* **2007**, *6*, 656−660.
(24) Dong, A.; Chen, J.; Vora, P. M.; Kikkawa, J. M.; Murray, C. B. Binary Nanocrystal Superlattice Membranes Self-Assembled at the Liquid-Air Interface. *Nature* **2010**, *466*, 474−477.
(25) Evers, W. H.; Nijs, B. D.; Filion, L.; Castillo, S.; Dijkstra, M.; Vanmaekelbergh, D. Entropy-Driven Formation of Binary Semiconductor-Nanocrystal Superlattices. *Nano Lett.* **2010**, *10*, 4235−4241.
(26) Pichler, S.; Bodnarchuk, M. I.; Kovalenko, M. V.; Yarema, M.; Springholz, G.; Talapin, D. V.; Heiss, W. Evaluation of Ordering in Single-Component and Binary Nanocrystal Superlattices by Analysis of Their Autocorrelation Functions. *ACS Nano* **2011**, *5*, 1703−1712.
(27) Marino, E.; Kodger, T. E.; Wegdam, G. H.; Schall, P. Revealing Driving Forces in Quantum Dot Supercrystal Assembly. *Adv. Mater.* **2018**, *30*, 1803433.
(28) Montanarella, F.; Geuchies, J. J.; Dasgupta, T.; Prins, P. T.; van Overbeek, C.; Dattani, R.; Baesjou, P.; Dijkstra, M.; Petukhov, A. V.; van Blaaderen, A.; et al. Crystallization of Nanocrystals in Spherical Confinement Probed by *In Situ* X-Ray Scattering. *Nano Lett.* **2018**, *18*, 3675−3681.
(29) Marino, E.; Keller, A. W.; An, D.; van Dongen, S.; Kodger, T. E.; MacArthur, K. E.; Heggen, M.; Kagan, C. R.; Murray, C. B.; Schall, P. Favoring the Growth of High-Quality, Three-Dimensional Supercrystals of Nanocrystals. *J. Phys. Chem. C* **2020**, *124*, 11256−11264.
(30) Bohren, C. F.; Huffman, D. R. *Absorption and Scattering of Light by Small Particles*; John Wiley & Sons: New York, 1983.
(31) Vanmaekelbergh, D.; van Vugt, L. K.; Bakker, H. E.; Rabouw, F. T.; Nijs, B. d.; van Dijk-Moes, R. J. A.; van Huis, M. A.; Baesjou, P. J.; van Blaaderen, A. Shape-Dependent Multiexciton Emission and Whispering Gallery Modes in Supraparticles of CdSe/Multishell Quantum Dots. *ACS Nano* **2015**, *9*, 3942−3950.
(32) Montanarella, F.; Altantzis, T.; Zanaga, D.; Rabouw, F. T.; Bals, S.; Baesjou, P.; Vanmaekelbergh, D.; van Blaaderen, A. Composite Supraparticles with Tunable Light Emission. *ACS Nano* **2017**, *11*, 9136−9142.
(33) Mie, G. Beiträge zur Optik trüber Medien, Speziell Kolloidaler Metallösungen. *Ann. Phys.* **1908**, *330*, 377−445.
(34) Kuznetsov, A. I.; Miroshnichenko, A. E.; Brongersma, M. L.; Kivshar, Y. S.; Luk'yanchuk, B. Optically Resonant Dielectric Nanostructures. *Science* **2016**, *354*, aag2472.
(35) Schäfer, J. Implementierung und Anwendung analytischer und numerischer Verfahren zur Lösung der Maxwellgleichungen für die Untersuchung der Lichtausbreitung in biologischem Gewebe. Ph.D. Thesis, Univerität Ulm, 2011.
(36) Diroll, B. T.; Gaulding, E. A.; Kagan, C. R.; Murray, C. B. Spectrally-Resolved Dielectric Functions of Solution-Cast Quantum Dot Thin Films. *Chem. Mater.* **2015**, *27*, 6463−6469.
(37) Grigoriev, V.; Bonod, N.; Wenger, J. m.; Stout, B. Optimizing Nanoparticle Designs for Ideal Absorption of Light. *ACS Photonics* **2015**, *2*, 263−270.
(38) Moosmüller, H.; Sorensen, C. Small and Large Particle Limits of Single Scattering Albedo for Homogeneous, Spherical Particles. *J. Quant. Spectrosc. Radiat. Transfer* **2018**, *204*, 250−255.
(39) Marino, E.; Kodger, T. E.; Crisp, R. W.; Timmerman, D.; MacArthur, K. E.; Heggen, M.; Schall, P. Repairing Nanoparticle Surface Defects. *Angew. Chem., Int. Ed.* **2017**, *56*, 13795−13799.
(40) Chen, W.; Guo, J.; Zhao, Q.; Gopalan, P.; Fafarman, A. T.; Keller, A.; Zhang, M.; Wu, Y.; Murray, C. B.; Kagan, C. R. Designing Strong Optical Absorbers *via* Continuous Tuning of Interparticle Interaction in Colloidal Gold Nanocrystal Assemblies. *ACS Nano* **2019**, *13*, 7493−7501.
(41) Liu, X.; Kent, N.; Ceballos, A.; Streubel, R.; Jiang, Y.; Chai, Y.; Kim, P. Y.; Forth, J.; Hellman, F.; Shi, S.; et al. Reconfigurable Ferromagnetic Liquid Droplets. *Science* **2019**, *365*, 264−267.
(42) Guo, J.; Kim, J.-Y.; Zhang, M.; Wang, H.; Stein, A.; Murray, C. B.; Kotov, N. A.; Kagan, C. R. Chemo- and Thermomechanically Configurable 3D Optical Metamaterials Constructed from Colloidal Nanocrystal Assemblies. *ACS Nano* **2020**, *14*, 1427−1435.
(43) Sychugov, I.; Pevere, F.; Luo, J.-W.; Zunger, A.; Linnros, J. Single-Dot Absorption Spectroscopy and Theory of Silicon Nanocrystals. *Phys. Rev. B: Condens. Matter Mater. Phys.* **2016**, *93*, 161413.
(44) Mann, S. A.; Sciacca, B.; Zhang, Y.; Wang, J.; Kontoleta, E.; Liu, H.; Garnett, E. C. Integrating Sphere Microscopy for Direct Absorption Measurements of Single Nanostructures. *ACS Nano* **2017**, *11*, 1412−1418.
(45) Mock, J. J.; Barbic, M.; Smith, D. R.; Schultz, D. A.; Schultz, S. Shape Effects in Plasmon Resonance of Individual Colloidal Silver Nanoparticles. *J. Chem. Phys.* **2002**, *116*, 6755−6759.
(46) Greybush, N. J.; Liberal, I.; Malassis, L.; Kikkawa, J. M.; Engheta, N.; Murray, C. B.; Kagan, C. R. Plasmon Resonances in Self-Assembled Two-Dimensional Au Nanocrystal Metamolecules. *ACS Nano* **2017**, *11*, 2917−2927.
(47) Losurdo, M.; Hingerl, K. *Ellipsometry at the Nanoscale*; Springer Science & Business Media: Berlin, 2013.
(48) High, A. A.; Novitskaya, E. E.; Butov, L. V.; Hanson, M.; Gossard, A. C. Control of Exciton Fluxes in an Excitonic Integrated Circuit. *Science* **2008**, *321*, 229−231.

https://dx.doi.org/10.1021/acsnano.0c06188
ACS Nano 2020, 14, 13806−13815

(49) Grosso, G.; Graves, J.; Hammack, A. T.; High, A. A.; Butov, L. V.; Hanson, M.; Gossard, A. C. Excitonic Switches Operating at around 100 K. *Nat. Photonics* **2009**, *3*, 577−580.
(50) Klimov, V. I. Spectral and Dynamical Properties of Multiexcitons in Semiconductor Nanocrystals. *Annu. Rev. Phys. Chem.* **2007**, *58*, 635−673.
(51) Kambhampati, P. Multiexcitons in Semiconductor Nanocrystals: A Platform for Optoelectronics at High Carrier Concentration. *J. Phys. Chem. Lett.* **2012**, *3*, 1182−1190.
(52) Klimov, V.; Hunsche, S.; Kurz, H. Biexciton Effects in Femtosecond Nonlinear Transmission of Semiconductor Quantum Dots. *Phys. Rev. B: Condens. Matter Mater. Phys.* **1994**, *50*, 8110−8113.
(53) Montanarella, F.; Biondi, M.; Hinterding, S. O. M.; Vanmaekelbergh, D.; Rabouw, F. T. Reversible Charge-Carrier Trapping Slows Förster Energy Transfer in CdSe/CdS Quantum-Dot Solids. *Nano Lett.* **2018**, *18*, 5867−5874.
(54) Won, R. Into the 'Mie-Tronic' era. *Nat. Photonics* **2019**, *13*, 585−587.
(55) Somerville, W. R. C.; Auguié, B.; Le Ru, E. C. SMARTIES: User-Friendly Codes for Fast and Accurate Calculations of Light Scattering by Spheroids. *J. Quant. Spectrosc. Radiat. Transfer* **2016**, *174*, 39−55.
(56) Palik, E. D. *Handbook of Optical Constants of Solids*; Academic Press: Burlington, 1997; Vol. *1*.

https://dx.doi.org/10.1021/acsnano.0c06188
ACS Nano 2020, 14, 13806−13815

Supporting information for

Simultaneous Photonic and Excitonic Coupling in Spherical Quantum Dot Supercrystals

Emanuele Marino,[†,‡] Alice Sciortino,[¶] Annemarie Berkhout,[§] Katherine E. MacArthur,[‖] Marc Heggen,[‖] Tom Gregorkiewicz,[†] Thomas E. Kodger,[⊥,†] Antonio Capretti,[†] Christopher B. Murray,[‡,#] A. Femius Koenderink,[§,†] Fabrizio Messina,[¶] and Peter Schall[*,†]

†*Van der Waals–Zeeman Institute, University of Amsterdam, Science Park 904, 1098XH, Amsterdam, The Netherlands*

‡*Department of Chemistry, University of Pennsylvania, 231 S. 34th St., 19104 Philadelphia (PA) , USA*

¶*Dipartimento di Fisica e Chimica–Emilio Segrè, Università degli Studi di Palermo, Via Archirafi 36, 90123 Palermo, Italy*

§*Center for Nanophotonics, AMOLF, Science Park 104, 1098XG Amsterdam, The Netherlands*

‖*Ernst Ruska Centre for Microscopy and Spectroscopy with Electrons and Peter Grünberg Institute, Forschungszentrum Jülich GmbH 52425 Jülich, Germany.*

⊥*Physical Chemistry and Soft Matter, Wageningen University and Research, Stippeneng 4, 6708WE, Wageningen, The Netherlands*

#*Department of Materials Science and Engineering, University of Pennsylvania, 220 S 33rd St., 19104 Philadelphia (PA), USA.*

E-mail: p.schall@uva.nl

Experimental details

Nanocrystal synthesis

Materials: All reagents are purchased from Sigma-Aldrich and are used as received.1-Octadecene (ODE, technical grade), oleic acid (OA, technical grade), CdO ($\geq$ 99.99% trace metals basis), selenium (powder $\sim$ 100 mesh, 99.99% trace metals basis), trioctylphosphine (TOP), hexane (reagent grade), and ethanol (200 proof, reagent grade).

Summary: CdSe nanocrystals were synthesized according to the recipe from Chernomordik *et al.*[1] with minor modifications. A brief description of the synthetic approach follows below.

Precursor preparation: A $1M$ TOP:Se complex is made by stirring $0.790g$ ($10mmol$) of Se powder in $10mL$ of TOP in a nitrogen-filled glovebox for overnight. All of the Se powder should be dissolved to form a transparent, yellow-tinted solution before use in the synthesis. Prior to synthesis, $3mL$ of the $1M$ TOP:Se is mixed with $7mL$ of ODE and loaded into a glass syringe placed in a syringe pump set for a rate of $10mL/hour$. The cadmium oleate precursor solution is prepared by mixing $0.512g$ of CdO, $6.28g$ of OA, and $25g$ of ODE ($32mL$) in a $100mL$ round-bottom flask. While stirring, the reagents are degassed at $100°C$ for one hour. Afterwards, the flask atmosphere is switched to nitrogen and the temperature is raised to $260°C$. The temperature is held constant until the color of the mixture changes from dark-red to colorless, indicating the formation of cadmium oleate. Subsequently, the temperature was dropped to $100°C$ and the flask was placed under vacuum for 30 minutes. This is done to remove the water produced during the reaction. After switching the atmosphere again to nitrogen, the temperature was raised to $260°C$. Meanwhile, $0.063g$ ($0.8mmol$) of Se powder is added to $5mL$ of ODE and sonicated for 20 minutes.

Nanocrystal synthesis: The Se/ODE mixture is injected at $260°C$ by using a $22mL$ plastic syringe equipped with a $16G$ needle. Immediately thereafter, the temperature controller is set to $240°C$. After 60 seconds from injection, the TOP:Se/ODE solution is added dropwise at a rate of $10mL/hour$. After 60 minutes, the reaction is quenched by removing the heating

mantle and dropping the flask in a container full of water at room-temperature. Note: the 1 hour time yields the nanocrystals with the lowest polydispersity. The reaction mixture is split into enough $50mL$ centrifuge tubes such that there are $5mL$ of mixture in each tube. Approximately $20mL$ of hexane is added to each tube and each tube is then capped and vortexed. $25mL$ of ethanol is added to each tube, and the tubes are centrifuged at $8000g$ for $5min$. Often, this first precipitation results in a slightly colored supernatant and it is discarded while keeping the precipitated QDs. The QD product is washed twice more by dispersing each QD precipitate in $10mL$ of hexane, and then precipitating with an equal volume of ethanol. After the final wash, the QD product is dispersed into hexanes at $50mg/mL$ and filtered by using a $200nm$ PTFE or PVDF syringe filter. Note: in absence of 200 proof ethanol, we suggest using a mixture of $3:1$ isopropanol:ethanol.

Small-angle X-ray scattering

Small angle X-ray scattering patterns were collected using a Pilatus 1M detector at BM26B beamline, DUBBEL at ESRF.[2–4] The duration of each measurement was set to 100 seconds collection time. The sample to detector distance was set to $2.9m$, achieving a q-range of $0.001 - 4nm^{-1}$. The beam energy was set to $12keV$.

The wavevector is defined as $q = 4\pi/\lambda \sin(\theta/2)$, where λ is the wavelength of incident X-rays and θ is the scattering angle. The form factor was extracted by fitting the experimental scattering pattern of diluted CdSe quantum dots in hexane to a spherical form factor F:

$$F(q,r) = 3V(r)\frac{(\sin(qr) - qr\cos(qr))}{(qr)^3}$$

where r is the particle radius and $V(r)$ is the volume of a sphere of radius r.[5] To account for size dispersion, we averaged over form factors of radius r varying around an average value r_0 where the contribution of each form factor was weighed with a Gaussian distribution $G(r, r_0, W)$ centered around $r = r_0$ and of width W. The result is:

$$F_G(q, r_0, W) = \int_0^{+\infty} F(q, r)^2 G(r, r_0, W) dr$$

The fitting procedure was performed either using self-developed code in Matlab, or using Sasfit software.[6] The polydispersity was calculated as $PD(\%) = 100W/(2r_0)$. The mean crystalline domain size ξ was determined through the Scherrer equation as $\xi = 2\pi K/\Delta q$, where $K = 1$ is the Scherrer constant for a spherical shaped crystals and Δq is the full-width at half-maximum of the 111 peak of the face-centered cubic diffraction pattern.[7]

Electron microscopy

For low resolution electron microscopy, we used a Verios XHR SEM microscope (FEI). The microscope was operated at $30kV$ and $100pA$. Bright field images, collected in transmission mode using a STEM detector, and secondary electron images, were collected simultaneously to investigate the internal and surface structure of the supercrystals, Figure S6 c-d. For high resolution electron microscopy, we used a Technai F20 TEM with field emission gun operating at $200kV$. The microscope has a 1.2mm Cs and is equipped with a Gatan UltranScan 1000P CCD camera. Magnification and focus were varied in order to yield information about the crystal structure and super structure of the particle sytems. In all cases, fast-Fourier transforms of the images were extracted by using ImageJ.

Mie theory

Software

Mie theory calculations on dielectric spheres were done using *MatScat*, an open source software available at https://nl.mathworks.com/matlabcentral/fileexchange/36831-matscat.[8] The Mie calculations of energy density and field were independently verified using finite element modelling (COMSOL Multiphysics 5.2). We also tested the behavior of Mie resonances for spheroids of different aspect ratios by using SMARTIES, another open source

software available at https://www.victoria.ac.nz/scps/research/research-groups/raman-lab/numerical-tools.[9]

Refractive index input

The complex refractive index for CdSe QDs was derived from ellipsometry data available in the literature by Diroll *et al.* for 5.1 nm CdSe QDs capped with oleic acid,[10] blue shifting the spectra by 8 nm to match the position of the first exciton peak in our samples. Specifically, the complex refractive index, $\tilde{n} = n + ik$, is reported in the supplementary spreadsheet of the publication of Diroll *et al.*, page 1, columns A (wavelength, λ), T (real part of the refractive index, n), and U (imaginary part of the refractive index, k).[10] The value of the refractive index used for the near-field simulations was: $\tilde{n}(\lambda = 400nm) = n + ik = 1.8173 + i0.0916$. The complex refractive index for silicon was also determined from the literature.[11]

Whispering gallery modes (WGM)

According to Mie theory, the largest superstructures in the ensemble studied in this work should display a number of whispering gallery modes (WGM). In a typical high index, micron-size Mie particle, the WGM are expected to be narrow (high quality factor), and sparse (large free spectral range). However, in between these sharp resonances, the response is dominated by broader features due to the non-resonant part of all the multipoles, and not by any particular WGM. At the slightest loss, deformation, or polydispersity the WGM signature would disappear. The QDs employed in this work are lossy, as the imaginary part of the refractive index is greater than zero, contributing in part to this effect. The study of individual superstructures allows us to exclude polydispersity as a cause for the disappearance of WGM resonances. In Figure S8, we investigate the role of the silicon substrate (a) and of the superstructures' aspect ratio (b). We show that even if the superstructures underwent a deformation to result in an aspect ratio lower than unity, the WGM resonances would shift but not disappear. However, the presence of the silicon substrate employed in

this study quickly results in the disappearance of these sharpest resonances as the guided modes leak into the high-index substrate. Using a lower refractive index material as support and QDs with a higher photoluminescence quantum yield should mitigate the absorption losses.

Photo-lithography

The mask was custom-made by Delta Mask b.v., Enschede (The Netherlands). The mask is made of quartz, with a chromium coating. 12 x 12 mm single-side polished silicon substrates were cleaned in acetone, sonicated in water, followed by cleaning with base piranha (15 minutes at 75 $^{\circ}C$), and a final 60s O2 plasma descum step (Oxford Instruments Plasma Technologies Plasmalab 80 Plus). Next the sample was spincoated with HMDS as adhesive layer, followed by spinning Ma-N1410 as optical resist. The target thickness was $1.5\mu m$. Next we exposed using a Suss Mask aligner MA BA 6(365 nm i-line) at a nominal dose of 325 mJ/cm^2. After development, the sample was evaporated with 15 nm of Cr after development using PVD (Polyteknik Flextura M508E) and lift-off was done in 1-methyl-2-pyrrolidone at $60^{\circ}C$.

Ensemble optical absorption measurements

Optical absorption spectra were measured using a Perkin Elmer Lambda 950 UV/Vis/NIR spectrophotometer with integrating sphere. A $5g/L$ dispersion of supercrystal in $6g/L$ sodium dodecyl sulfate in water was drop-casted on a quartz substrate. The measurement was performed by placing the substrate at the front of the integrating sphere, so to allow for the collection of transmitted and forward-scattered light.

Single supercrystal dark-field microscopy

We perform reflective dark field microscopy using a home-built setup that is based on a Nikon universal illuminator unit (Nikon LV-UEPI 2 system) and a $100W$ halogen lamp, equipped with objectives from the CFI LU Plan Fluor BD series (20x NA 0.45 , 50x NA 0.8, and 100x NA 0.9). Samples are imaged with a $f = 200mm$ achromatic tube lens. Directly after the tube lens, a 70/30 beam splitter (Thorlabs BS022) directs 70% of the light onto the entrance facet of a collection fiber, while the remaining 30% is used to form an image on a CMOS color camera (Imaging Source DFK 21AU04). The collection fiber (Thorlabs M16L01, $50\mu m$ core, NA 0.22) is multi-mode, and leads to an Avaspec 2048TEC-2-USB2 spectrometer (thermo-electrically cooled 2048 pixel Si CCD, $600l/mm$ grating, $75mm$ focal length). This spectrometer has a resolving power of around $0.3nm/pixel$ and a detection range from 500 to 1000 nm. No polarization optics are used. Spectra in this work are taken with the 100x objective, with illumination through the objective reflective mantle at angles just beyond the collection NA.

Sample preparation consisted in 2 minutes of plasma cleaning of the lithographically-patterned substrates, followed by spin-coating ($1500rpm$, $30s$ and $3000rpm$, $10s$) of a dispersion of CdSe QD supercrystals ($5 \times 10^{-3}g/L$) in water (sodium dodecyl sulfate $6g/L$).

The measurement protocol consisted of:

- finding a supercrystal previously imaged by SEM using the lithographically patterned substrate;
- focusing and collecting the dark field signal from the supercrystal by integrating for a time Δt: $I_{sample}(\lambda, \Delta t)$;
- collecting the reference dark field signal from the silicon substrate in proximity of the location of the supercrystal: $I_{substrate}(\lambda, \Delta t')$;
- calculating the background subtracted signal from the supercrystal as: $I_{sample,bs} = I_{sample}(\lambda, \Delta t)/\Delta t - I_{substrate}(\lambda, \Delta t')/\Delta t'$

- correcting for the wavelength-dependence of the source, optics, and CCD by measuring the dark field signal from a broad-band light-scattering target, namely a glass coverslip coated with a thick layer of white paint for integrating spheres: $I_{ref,bs} = I_{ref}(\lambda, \Delta t'')/\Delta t'' - I_{substrate}(\lambda, \Delta t')/\Delta t'$. The corrected dark-field signal from the supercrystal then reads: $I_{sample,corrected} = I_{sample,bs}/I_{ref,bs}$.

Transient absorption

Femtosecond transient absorption (TA) measurements were based on a 5 kHz Ti:sapphire femtosecond amplifier (Spectra Physics Solstice-Ace) which produces 75 fs pulses peaking at $\lambda = 800nm$ (FWHM=30 nm) at $350\mu J$/pulse. This beam is split in two parts by a beam splitter (80%/20%) to generate the pump and the probe, respectively. The pump ($\lambda = 400nm$) is produced by frequency-doubling the fundamental $\lambda = 800nm$ (type I phase-matching) in a $250\mu m$ β-BBO crystal. The pump beam is chopped at 500 Hz and focused on a $200\mu m$ light path quartz flow cell by a parabolic mirror with f=150 mm. Its polarization is controlled by a waveplate. A probe beam consists of a supercontinuum pulse ($\lambda = 400 - 700nm$) generated by focusing the $\lambda = 800nm$ beam on a D_2O-filled $1mm$ light path quartz cuvette. The probe is focused on the sample by the same parabolic mirror used to focus the pump. The pump-probe delay is controlled by a motorized delay stage which yields a temporal resolution of 70 fs. The probe and the pump overlap within the same portion of the sample. After the sample, the probe beam is dispersed through a Brewster-angle silica prism and focused on the detector by a lens. The spectral resolution is 3 nm. Pump and probe are synchronized with a camera detector system with 1024 pixels (Glaz Linescan-I) with single-shot capability. A typical signal is obtained by averaging 5000 pumped and 5000 unpumped spectra for each delay, and scanning over the pump-probe delay 40 times. A schematic of the setup is shown in Figure S9.

Supplementary figures

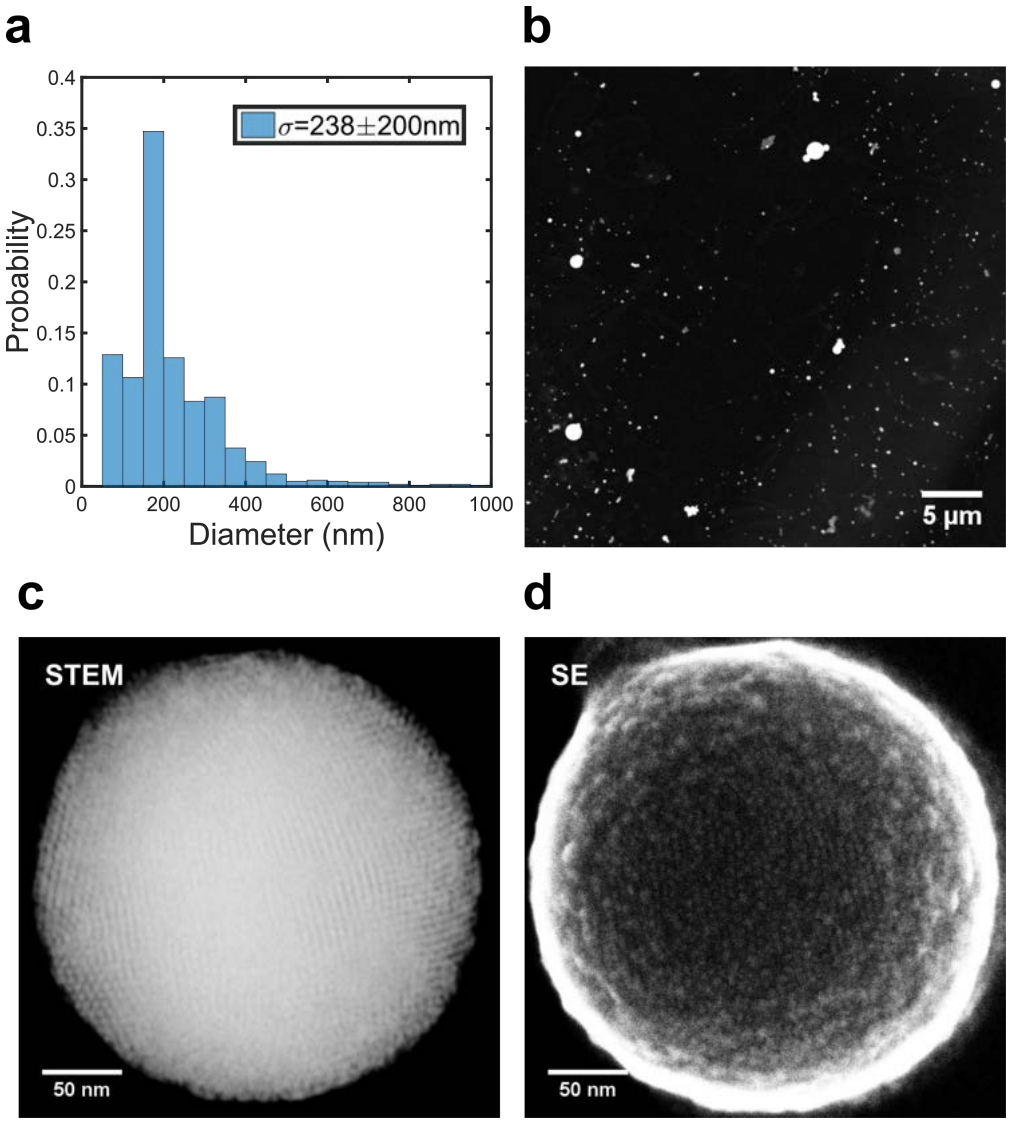

Figure S1: **QD supercrystals.** (a) Histogram of the diameters of QD supercrystals as determined by the dark-field STEM micrograph shown in (b). Dark-field STEM (c) and secondary electron (d) micrographs of a single supercrystal showing supercrystal fringes and surface details, respectively.

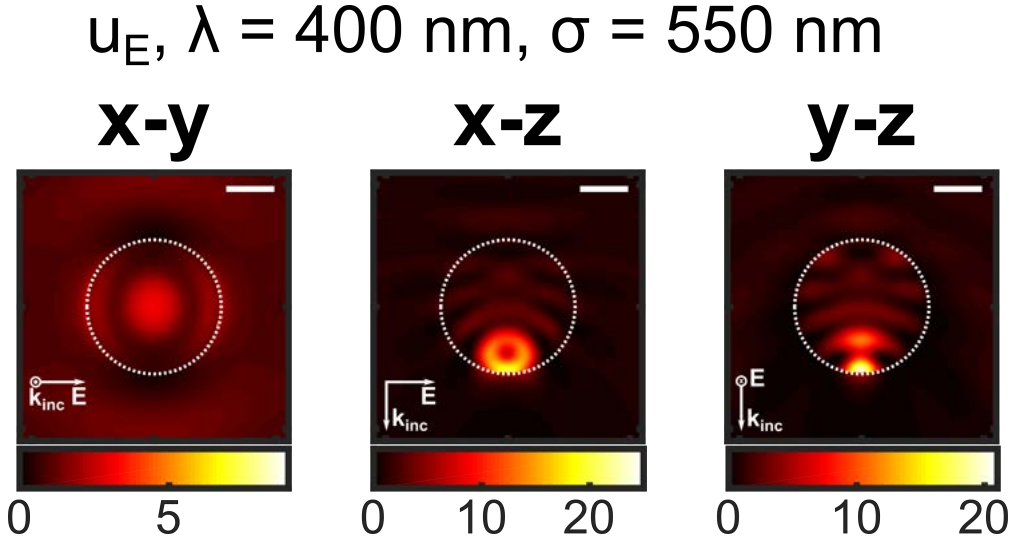

Figure S2: Map of the electric field energy density, $u_E \sim n(\lambda)^2|\mathbf{E}|^2$, within and in proximity of a QD supercrystal of diameter $\sigma = 550nm$ for $\lambda = 400nm$. The geometric cross section of supercrystal is outlined by a dotted white line. The directions of the incident plane wave, $\mathbf{k_{inc}}$, and of the electric field, $\mathbf{E}$, are specified for three different planes. Scale bars indicate $\lambda/2$.

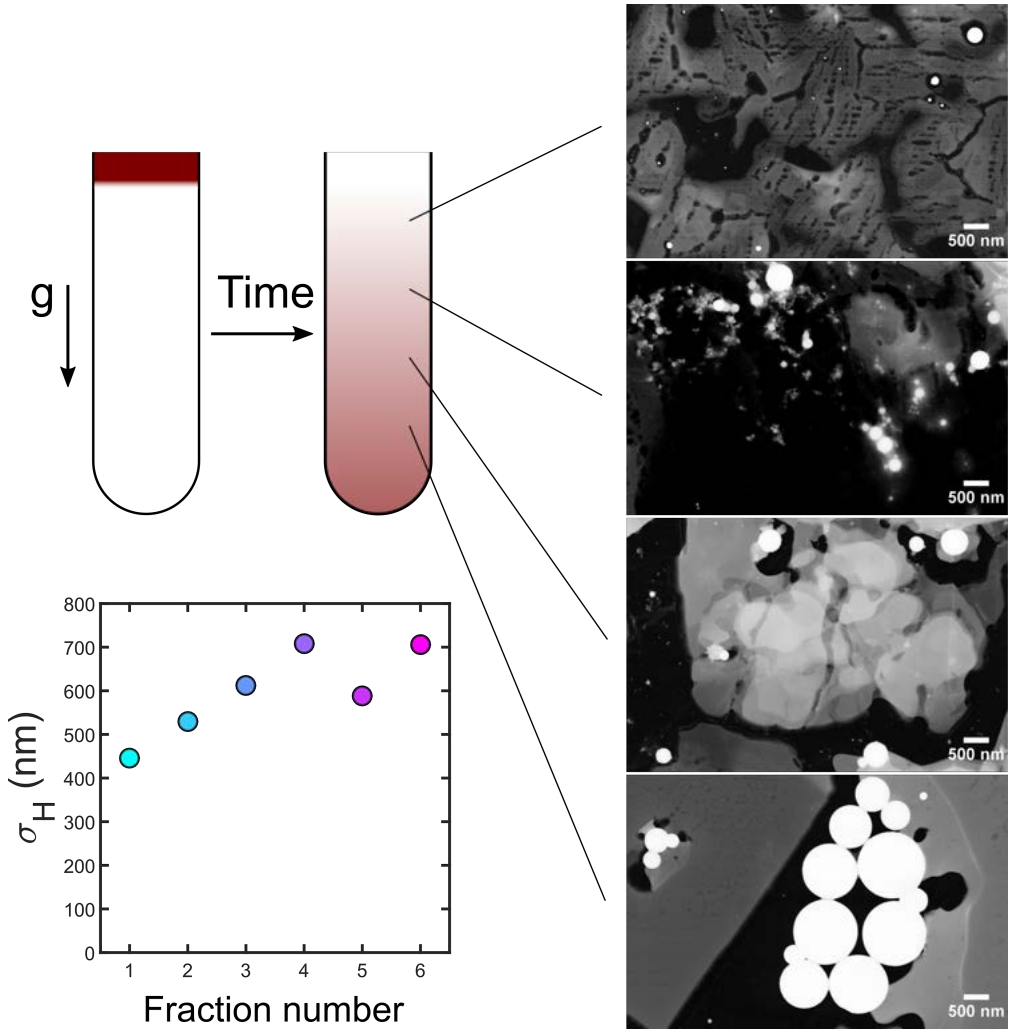

Figure S3: **Size-fractionation of QD supercrystals.** (Top left) A dispersion of polydisperse QD supercrystals in $6g/L$ sodium dodecyl sulfate, SDS, in water is gently layered on a $1:1v/v$ mixture of water and glycerol, $6g/L$ SDS. Under the effect of gravity, the polydisperse supercrystals separate according to size. The fractions were collected after 1 hour of fractionation by gently removing $1mL$ of dispersion per fraction from the top of the mixture. The excess glycerol was removed by 3 cycles of centrifugation and redispersion in $6g/L$ SDS in water. (Right) SEM micrographs of fractions of increasing average size of QD supercrystals. (Bottom left) Average hydrodynamic diameter, σ_H, measured with dynamic light scattering (DLS) on the collected fractions. The average size of supercrystals increases with fraction number until saturation. The saturation is likely due to the dominance of sedimentation over diffusion of the largest supercrystals whose size cannot therefore be estimated by using DLS.

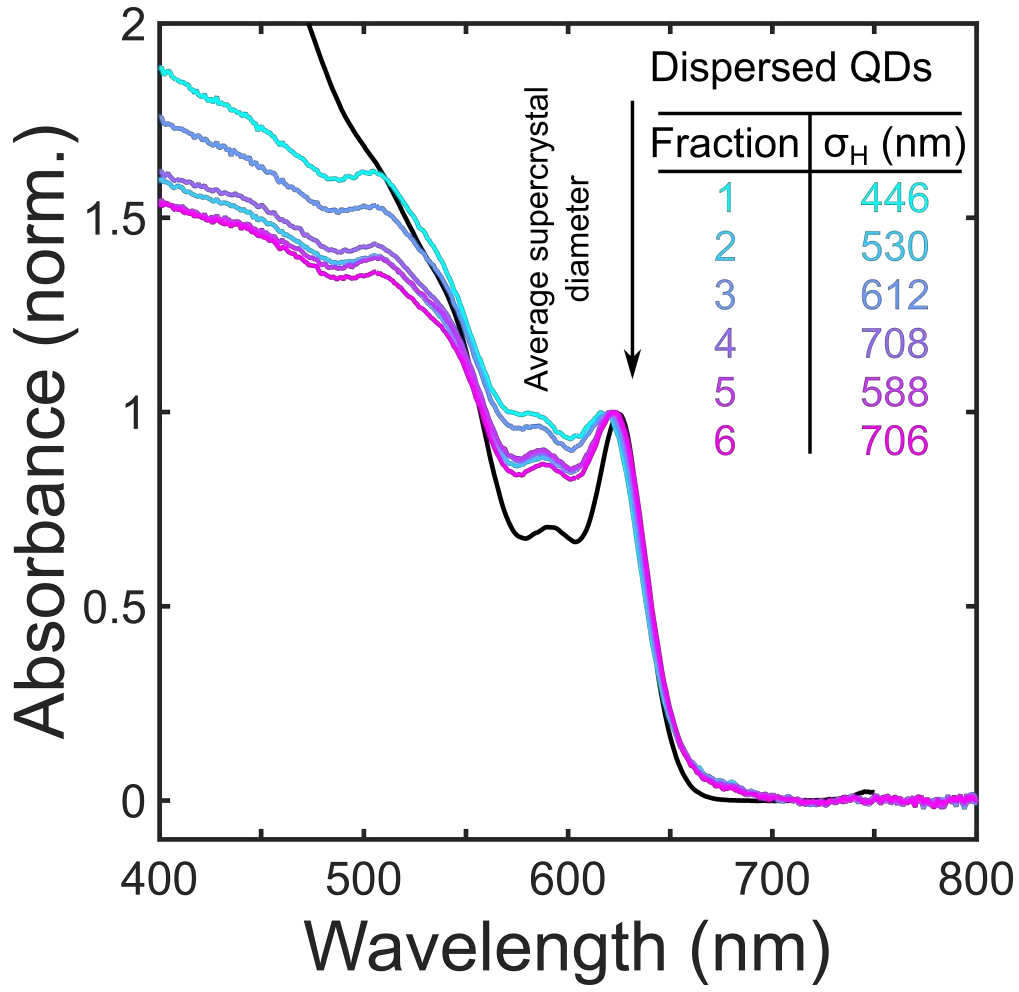

Figure S4: **Absorption spectra of size-fractionated QD supercrystals.** Details of the fractionation process are reported in Figure S3.The absorption spectrum of dispersed QDs is also reported for reference (solid black line).

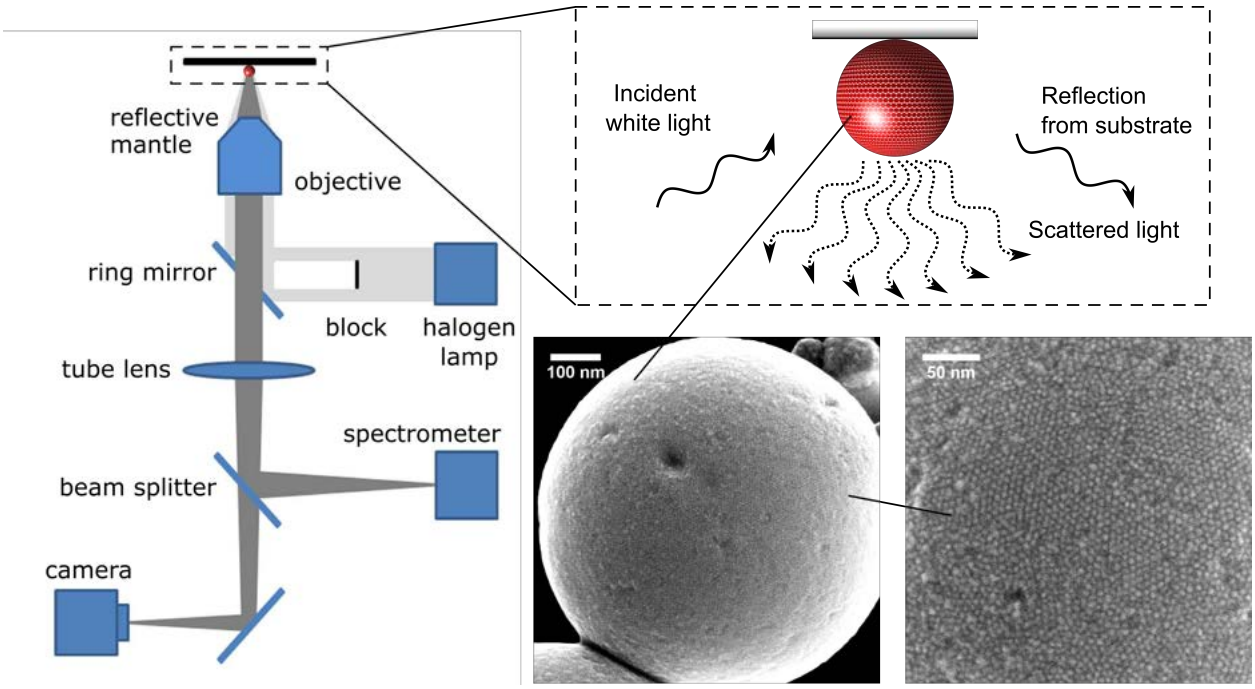

Figure S5: **Simplified dark-field setup schematic.** (Left and top-right) Schematics of setup's geometry. An incident beam of white light impinges at an angle θ_i on the QD supercrystals deposited on a silicon substrate. The collection angle $\theta_c < \theta_i$ purposely misses the reflected beam to allow for a dark-field measurement. (Bottom-right) Reresentative SEM micrographs of a QD supercrystal at intermediate (left) and high (right) magnifications.

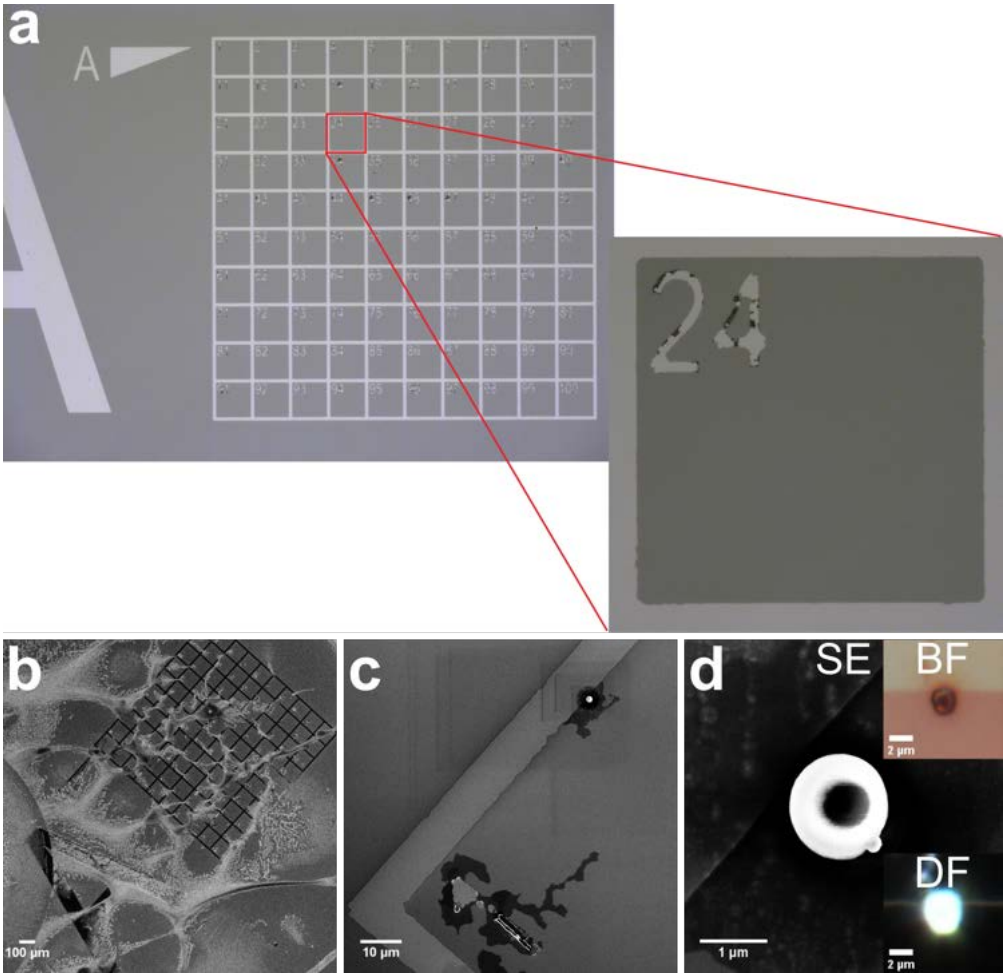

Figure S6: **Photo-lithographically patterned silicon substrate used to correlate optical properties of individual supercrystals (measured using dark-field microscopy, DF) with their diameters (measured using scanning electron microscopy, SEM).** (a) Overview of the checkerboard pattern labeled 'A'. The light areas describe a $3nm$ layer of chromium sputtered on silicon. Each square has a side of $100\mu m$ and each side is $10\mu m$ wide. (b) The same checkerboard pattern after spin-coating a $0.005g/L$ dispersion of CdSe supercrystals in $6g/L$ sodium dodecyl sulfate in water. Excess surfactant is visible on the substrate. (c) Detail of the square labeled 'A1'. A single supercrystal is visible at the top of the image. (d) Detail of the supercrystal. Supercrystal diameter: $\sigma = 1480nm$. The insets show images of the same supercrystal collected under bright field (BF) and dark field conditions.

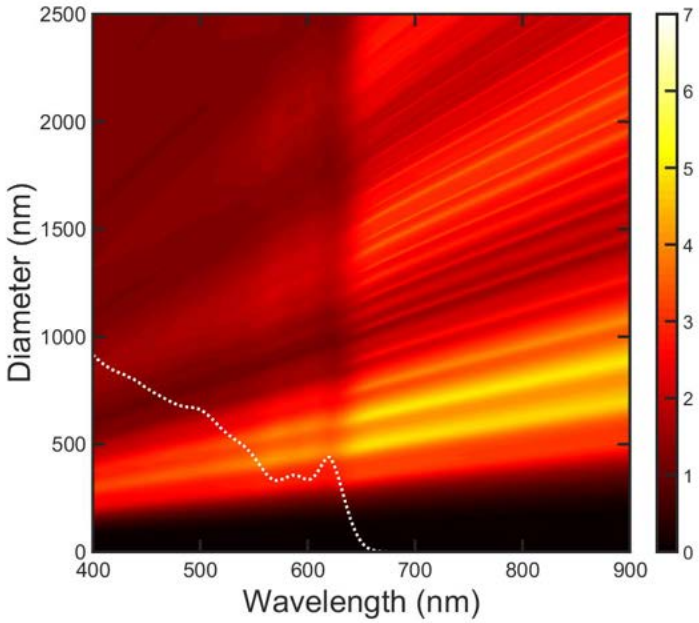

Figure S7: Map of the scattering efficiency of CdSe QD supercrystals as a function of excitation wavelength, λ, and supercrystal diameter, σ, as modeled from Mie theory. The dotted white line describes the imaginary part of the refractive index of QDs used in the modeling, k,

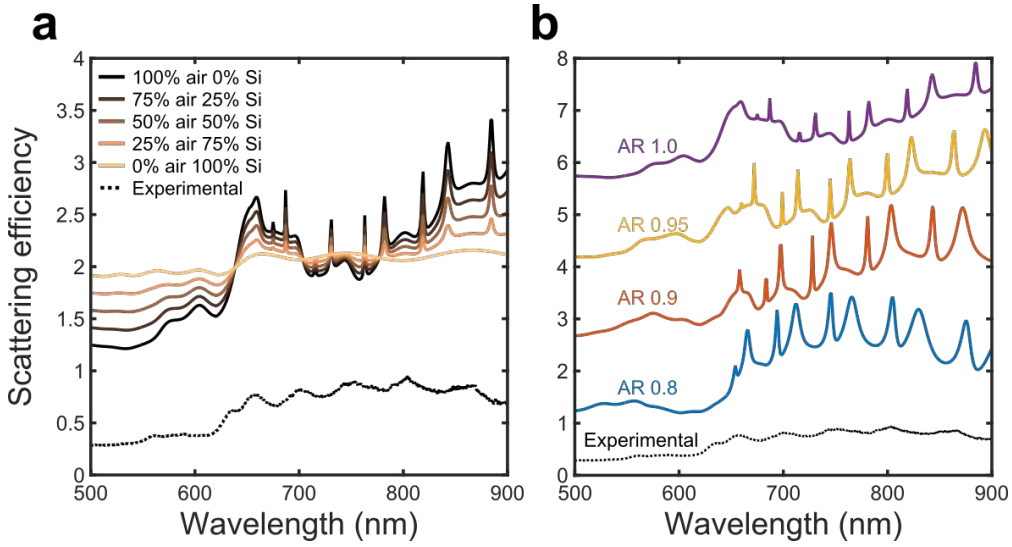

Figure S8: **Effects of surrounding medium and aspect ratio on the scattering cross section of individual QD supercrystals.** (a) We modeled the influence of the silicon substrate by calculating the absorption cross section of a supercrystal embedded respectively in air and silicon, and performing a weighted average to simulate the experimental condition of a supercrystal in air deposited on a silicon substrate. The presence of a silicon medium in proximity of the supercrystal dampens the sharper resonances of the spectrum. This likely explains why we do not observe these sharper resonances experimentally. (b) Altering the aspect ratio of the supercrystals alters the theoretical scattering cross section. A 5% deviation from 1 already causes a significant shift in the peak position of the resonances, while also broadening the local minimum corresponding to the first exciton peak of the nanocrystals. Since we do not observe neither of these conditions, we conclude that the aspect ratio is not altered by deposition of the supercrystal on a substrate. Supercrystal diameter, calculated as the average of the long and short axes of the ellipsoid: $\sigma = 2187nm$.

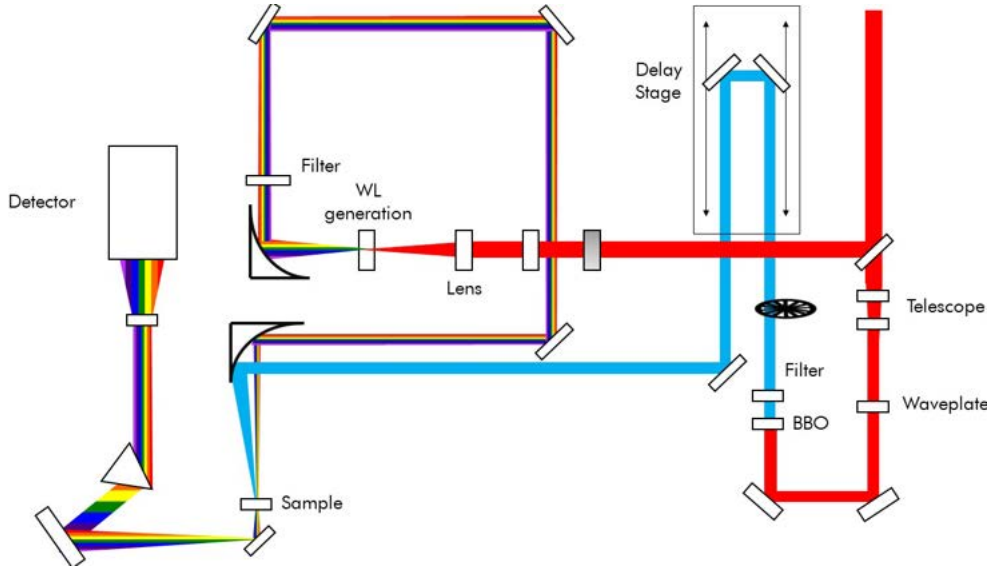

Figure S9: **Schematic of the experimental setup of transient absorption ultrafast spectroscopy.** The ultrafast $800nm$ pulses generated by a Ti:sapphire laser are split by a $80\% - 20\%$ beamsplitter. The high power beam is doubled in frequency by using a BBO crystal and used to pump the sample. The low power beam is used to generate the white light probe beam. The dispersion of supercrystals is continously flowed through a microfluidic cell to avoid irradiation-induced sample damage.

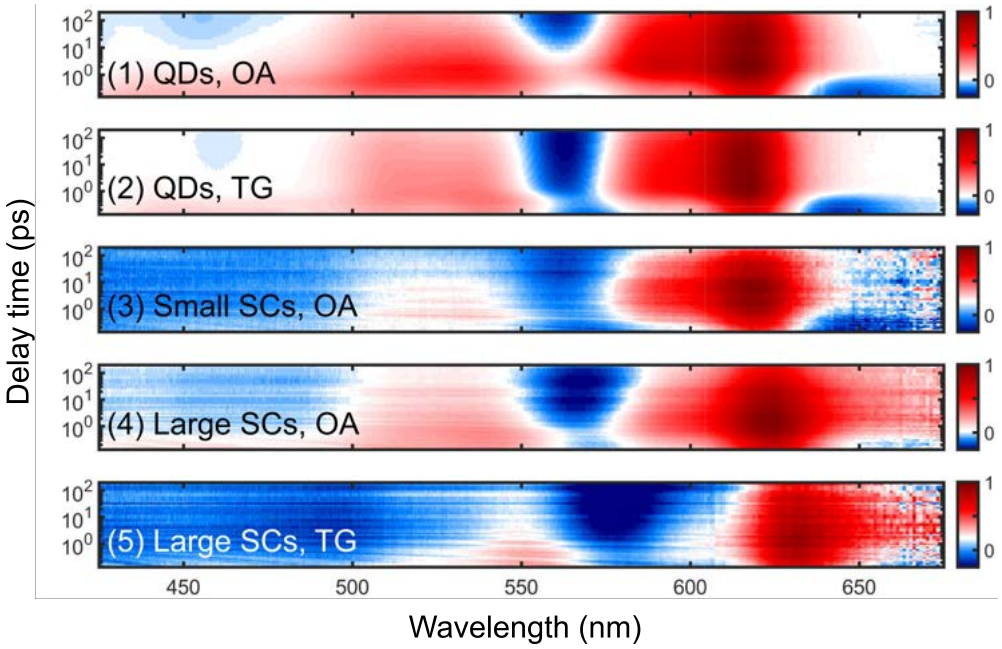

Figure S10: 2D maps of the normalized negative transient-absorption signal relative to the samples treated in the main text.

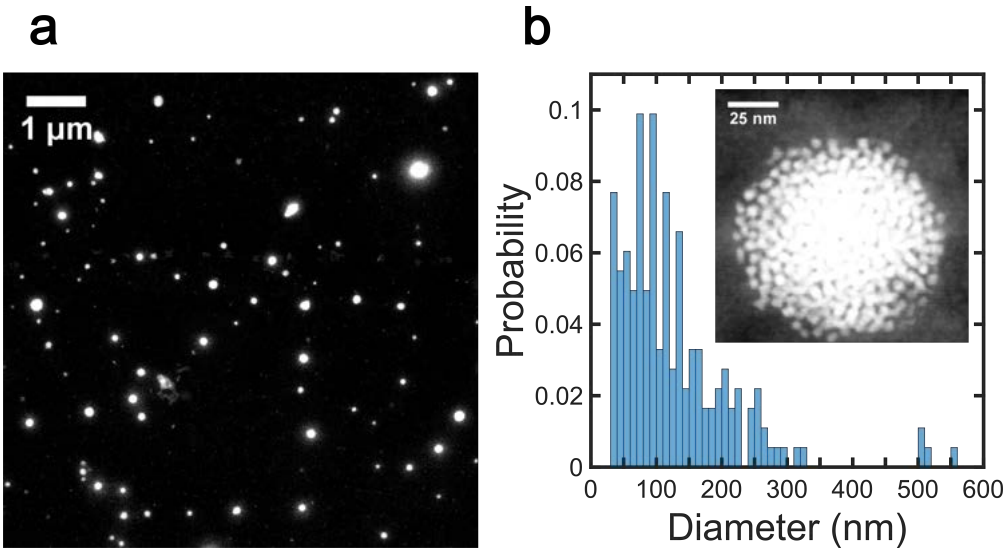

Figure S11: **Size-separated SCs with the smallest diameters available.** (a) Low-magnification scanning electron micrograph of size-separated QD supercrystals of the smallest average size available. These supercrystals were size-separated by centrifuging the dispersion of polydisperse supercrystals at $10000g$ for $10min$. (b) Histogram of supercrystal diameters. Average diameter: $130nm$. (Inset) Close-up of an individual QD supercrystal of $\sim 100nm$ diameter.

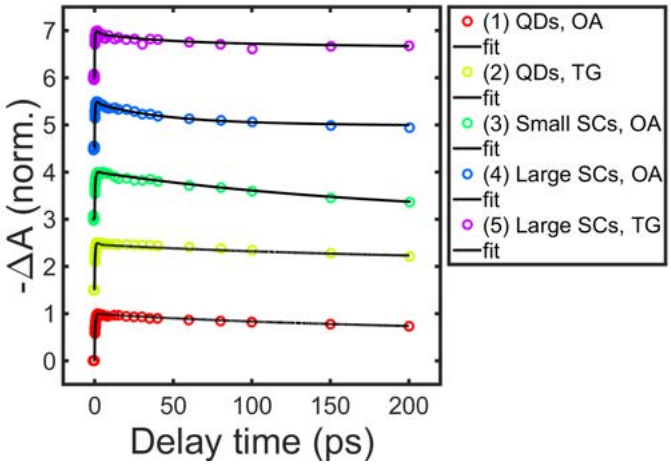

Figure S12: **Cooling kinetics for the samples discussed in the main text.** Pump-probe kinetics traces recorded at $\lambda = 620nm$ with the least-squares fitting curves for all samples discussed in the main text. The kinetics are fit to a superposition of four exponential components $\sum_{i=1}^{i=4} A_i \exp(-t/\tau_i)$ of which the fastest one describes state filling (exponential rise) and the slower ones describe charge carrier recombination (exponential decays). The time constant describing state filling amounts to $\tau = 0.7ps$ for samples 1,2,3,5, and $0.6ps$ for sample 4.

References

1. Chernomordik, B. D.; Marshall, A. R.; Pach, G. F.; Luther, J. M.; Beard, M. C. Quantum Dot Solar Cell Fabrication Protocols. *Chem. Mater.* **2017**, *29*, 189–198.

2. Marino, E.; Kodger, T. E.; Wegdam, G. H.; Schall, P. Revealing Driving Forces in Quantum Dot Supercrystal Assembly. *Adv. Mater.* **2018**, *30*, 1803433.

3. Portale, G.; Cavallo, D.; Alfonso, G. C.; Hermida-Merino, D.; Drongelen, M. v.; Balzano, L.; Peters, G. W. M.; Goossens, J. G. P.; Bras, W. Polymer Crystallization Studies under Processing-Relevant Conditions at the SAXS/WAXS DUBBLE Beamline at the ESRF. *J. Appl. Crystallogr.* **2013**, *46*, 1681–1689.

4. Bras, W.; Dolbnya, I. P.; Detollenaere, D.; Tol, R. v.; Malfois, M.; Greaves, G. N.; Ryan, A. J.; Heeley, E. Recent Experiments on a Small-Angle/Wide-Angle X-Ray Scattering Beam Line at the ESRF. *J. Appl. Crystallogr.* **2003**, *36*, 791–794.

5. Pedersen, J. S. Analysis of Small-Angle Scattering Data from Colloids and Polymer Solutions: Modeling and Least-Squares Fitting. *Adv. Colloid Interface Sci.* **1997**, *70*, 171–210.

6. Breßler, I.; Kohlbrecher, J.; Thünemann, A. F. SASfit: A Tool for Small-Angle Scattering Data Analysis Using a Library of Analytical Expressions. *J. Appl. Crystallogr.* **2015**, *48*, 1587–1598.

7. Schöpe, H. J.; Bryant, G.; van Megen, W. Effect of Polydispersity on the Crystallization Kinetics of Suspensions of Colloidal Hard Spheres when Approaching the Glass Transition. *J. Chem. Phys.* **2007**, *127*, 084505.

8. Schäfer, J. Implementierung und Anwendung analytischer und numerischer Verfahren zur Lösung der Maxwellgleichungen für die Untersuchung der Lichtausbreitung in biologischem Gewebe. Ph.D. thesis, Univerität Ulm, 2011.

9. Somerville, W. R. C.; Auguié, B.; Le Ru, E. C. SMARTIES: User-Friendly Codes for Fast and Accurate Calculations of Light Scattering by Spheroids. *J. Quant. Spectrosc. Radiat. Transfer* **2016**, *174*, 39–55.

10. Diroll, B. T.; Gaulding, E. A.; Kagan, C. R.; Murray, C. B. Spectrally-Resolved Dielectric Functions of Solution-Cast Quantum Dot Thin Films. *Chem. Mater.* **2015**, *27*, 6463–6469.

11. Palik, E. D. *Handbook of Optical Constants of Solids*; Academic press: Burlington, 1997; Vol. 1.